ELEMENTA
Science of the Anthropocene

Lonardi, M, et al. 2022. Tethered balloon-borne profile measurements of atmospheric properties in the cloudy atmospheric boundary layer over the Arctic sea ice during MOSAiC. *Elem Sci Anth*, 10: 1. DOI: https://doi.org/10.1525/elementa.2021.000120

RESEARCH ARTICLE

Tethered balloon-borne profile measurements of atmospheric properties in the cloudy atmospheric boundary layer over the Arctic sea ice during MOSAiC: Overview and first results

Michael Lonardi[1,*], Christian Pilz[2], Elisa F. Akansu[2], Sandro Dahlke[3], Ulrike Egerer[2,4,5], André Ehrlich[1], Hannes Griesche[2], Andrew J. Heymsfield[6], Benjamin Kirbus[1], Carl G. Schmitt[7], Matthew D. Shupe[4,8], Holger Siebert[2], Birgit Wehner[2], and Manfred Wendisch[1]

The tethered balloon-borne measurement system BELUGA (Balloon-bornE moduLar Utility for profilinG the lower Atmosphere) was deployed over the Arctic sea ice for 4 weeks in summer 2020 as part of the Multidisciplinary drifting Observatory for the Study of Arctic Climate expedition. Using BELUGA, vertical profiles of dynamic, thermodynamic, aerosol particle, cloud, radiation, and turbulence properties were measured from the ground up to a height of 1,500 m. BELUGA was operated during an anomalously warm period with frequent liquid water clouds and variable sea ice conditions. Three case studies of liquid water phase, single-layer clouds observed on 3 days (July 13, 23, and 24, 2020) are discussed to show the potential of the collected data set to comprehensively investigate cloud properties determining cloud evolution in the inner Arctic over sea ice. Simulated back-trajectories show that the observed clouds have evolved within 3 different air masses ("aged Arctic," "advected over sea ice," and "advected over open ocean"), which left distinct fingerprints in the cloud properties. Strong cloud top radiative cooling rates agree with simulated results of previous studies. The weak warming at cloud base is mostly driven by the vertical temperature profile between the surface and cloud base. In-cloud turbulence induced by the cloud top cooling was similar in strength compared to former studies. From the extent of the mixing layer, it is speculated that the overall cloud cooling is stronger and thus faster in the warm oceanic air mass. Larger aerosol particle number concentrations and larger sizes were observed in the air mass advected over the sea ice and in the air mass advected over the open ocean.

Keywords: Tethered balloon, Profile, Arctic, Atmospheric boundary layer, Cloud, MOSAiC

[1] Leipzig Institute for Meteorology (LIM), Leipzig University, Leipzig, Germany

[2] Department of Experimental Aerosol and Cloud Microphysics, Leibniz Institute for Tropospheric Research (TROPOS), Leipzig, Germany

[3] Helmholtz Centre for Polar and Marine Research, Alfred Wegener Institute (AWI), Potsdam, Germany

[4] Cooperative Institute for Research in Environmental Sciences (CIRES), University of Colorado, Boulder, CO, USA

[5] National Snow and Ice Data Center (NSIDC), University of Colorado Boulder, Boulder, CO, USA

[6] National Center for Atmospheric Research (NCAR), Boulder, CO, USA

[7] Geophysical Institute, University of Alaska, Fairbanks, AK, USA

[8] Physical Sciences Laboratory (PSL), National Oceanic and Atmospheric Administration (NOAA), Boulder, CO, USA

* Corresponding author:
Email: michael.lonardi@uni-leipzig.de

1. Introduction

The currently observed drastic climate changes in the Arctic are the result of an enhanced sensitivity of the Arctic climate system to a multitude of intertwined impact factors. This phenomenon is known as Arctic amplification (Serreze and Barry, 2011). The most obvious indications of Arctic amplification are the increase of near-surface air temperature (Bekryaev et al., 2010; Box et al., 2019; Moon et al., 2021) and the dramatic retreat of sea ice (Stroeve and Notz, 2018; Box et al., 2019). They are the consequence of a complex system of local and remote processes and feedback mechanisms (Serreze and Barry, 2011; Taylor et al., 2013; Pithan and Mauritsen, 2014; Wendisch et al., 2017), which include the local surface albedo, lapse rate, water vapor, and cloud feedback mechanisms, as well as remote processes, such as synoptically driven meridional advection of warm, humid, and polluted air from midlatitudes into the Arctic or cold air outbreaks.

Models partly disagree in representing the processes driving Arctic amplification (Serreze and Francis, 2006; Ceppi et al., 2017; Cohen et al., 2020), which may be caused by a lack of understanding of the relevant atmospheric processes. This deficiency underlines the need to constrain the model results using observations.

Low-level Arctic clouds play a decisive role in several feedback mechanisms driving Arctic amplification (Wendisch et al., 2019). They absorb and emit thermal-infrared radiation (TIR) and scatter/absorb solar radiation. They influence the surface radiative energy flux densities (irradiances) and modulate temperature profiles. In turn, the vertical temperature profile determines the emission of TIR and is intimately related to cloud vertical extent and other properties. Cloud top radiative cooling generates turbulence that drives the vertical transport and mixing associated with the cloud (Morrison et al., 2012). The entrainment of cloud condensation nuclei (CCN) and moist air into the cloud regulates cloud evolution. These interactions make Arctic cloud properties highly variable, especially when temperature and humidity profiles, as well as the amount of CCN, are modified during long-range transport of air masses (Pithan et al., 2018).

The sea ice covered Arctic ocean hampers comprehensive and continuous ground-based observations in the central Arctic. Therefore, dedicated campaigns using icebreaking ships and aircraft are employed (Wendisch et al., 2019; Shupe et al., 2022). In recent years, measurements by uncrewed aerial vehicles (de Boer et al., 2018; Lampert et al., 2020) and tethered balloon-borne observations (Dexheimer et al., 2019; Egerer et al., 2019; Ferrero et al., 2019; Creamean et al., 2021; Egerer et al., 2021) were performed to collect data in the Arctic. Egerer et al. (2019) and Egerer et al. (2021) obtained vertical profile measurements of combined atmospheric turbulence and radiative parameters with the tethered balloon measurement system BELUGA (Balloon-bornE moduLar Utility for profilinG the lower Atmosphere).

Here, we report on the first results of measurements with BELUGA obtained during the year-long Multidisciplinary drifting Observatory for the Study of Arctic Climate (MOSAiC) expedition (Shupe et al., 2022). BELUGA was operated from an ice camp during a 4-week period in summer 2020. The BELUGA deployment generally aimed at characterizing local atmospheric processes and assessing their importance with respect to remote forcings. We specifically focus on analyzing the vertical structure of broadband radiation, turbulence, aerosol, and microphysical properties under the influence of different temperature profiles and advected air masses. Furthermore, we were looking for the footprint of air mass characteristics in the cloud properties. The BELUGA observations were used to characterize the atmospheric boundary layer (ABL) over the central Arctic sea ice and to bridge the gap between regular radio soundings and continuous remote sensing of the ABL (Shupe et al., 2022). Remote sensing of cloud and aerosol properties by lidar and radar served to link the sporadic balloon observations to the surface-based continuous time series.

In Section 2, the application of BELUGA during the MOSAiC expedition is introduced. In Section 3, synoptic weather conditions prevailing during the deployment period and local observations are described. Examples of measured profiles through liquid water phase, single-layer clouds conducted during 3 days (July 13, 23, and 24, 2020) are presented and discussed in Section 4. The analysis covers back-trajectories of air masses, temperature, cloud microphysical properties, broadband (solar and TIR) irradiances, wind, turbulence, and aerosol properties. Section 5 summarizes the conclusions of this study.

2. BELUGA instrumentation and operation during MOSAiC

BELUGA consists of a helium-filled tethered balloon and an adaptable instrument payload specifically designed to minimize the weight of the instruments and to guarantee a stable horizontal sensor alignment during operation (Egerer et al., 2019). The balloon allows for the deployment of multiple sensors. The original instrument setup of BELUGA (Egerer et al., 2019) was optimized and extended for operation during MOSAiC by implementing improved instrument versions and by adding two new probes. Furthermore, a new balloon with enhanced buoyancy was applied. **Table 1** summarizes the instrument packages operated during MOSAiC, the measured quantities, and derived products, including an estimate of the uncertainty.

Standard meteorological parameters were measured with an extended meteorological package (EP) combining a modified radiosonde and a Pitot tube. The system was recalibrated in a wind tunnel at constant pressure to correct the wind speed measurements. Three-dimensional wind and virtual air temperature were recorded by an ultrasonic anemometer package (UP) to derive the local energy dissipation rate ε. Downward and upward TIR and solar radiative flux densities (irradiances) were measured by a broadband radiation package (BP) that combined pyrgeometers and pyranometers. Irradiances were corrected for the time response of the radiometer and averaged over 3 s. Net irradiances were derived by the difference between downward and upward irradiances. TIR heating rates were obtained from 20-m vertical segments following the method illustrated by Egerer et al. (2019). Before any processing, EP, UP, and BP measurements were corrected for the tilt of the sensors with respect to the horizontal reference plane during flight. The Cubic Aerosol Measurement Platform (Pilz et al., 2022) measured number concentration of particles larger than 12 nm (N_{12}) with a condensation particle counter. An optical particle size spectrometer measured particle number size distribution (PNSD) of particles between 0.15 and 2.9 μm and the integrated particle number concentration ($N_{>150}$). The number concentration of particles between 12 and 150 nm (N_{12-150}) was calculated by the difference of the two concentrations. A balloon version of the Video Ice Particle Sampler (VIPS; Heymsfield and McFarquhar, 1996) was applied to record cloud droplet and ice

Table 1. Instrumental setup

Instrument	Model, Manufacturer	Measured Quantity	Uncertainty	Inferred Quantity	Uncertainty
Extended meteorological package, EP					
Radiosonde	DFM-17, GRAW (Nürnberg, DE)	Temperature, T	0.2 K		
		Relative humidity, RH	3%–5%		
Pitot-static tube		Wind speed, WS	0.5 m s^{-1}		
3-Axis compass	HMC6343, Honeywell (Plymouth, MN, USA)	Wind direction, WD	5°		
Ultrasonic anemometer package, UP					
Ultrasonic anemometer	uSonic-3 Class A, Metek (Elmshorn, DE)	3-D wind vector	7.5 cm s^{-1} 1.5°	Local energy dissipation rate, ε	15%
Broadband radiation package, BP					
Pyrgeometer (2x)	CGR4, Kipp & Zonen (Delft, NL)	Downward TIR irradiance	5 Wm^{-2}	Net TIR irradiance, *Fnet*	7 Wm^{-2}
		Upward TIR irradiance	5 Wm^{-2}	TIR heating rate, ζ	12 K day^{-1}
Pyranometer (2x)	CMP3, Kipp & Zonen	Downward solar irradiance	2%		
		Upward solar irradiance	2% (below cloud), 5% (above cloud)		
Cubic Aerosol Measurement Platform, CAMP					
Condensation particle counter	CPC 3007 (modified), TSI (Shoreview, MN, USA)	Particle number concentration, $N_{12\ nm}$	5%	Particle number concentration, $N_{12-150\ nm}$	10%
Condensation particle counter	CPC 3007 (modified), TSI	Particle number concentration, $N_{>150\ nm}$	5%		
Optical particle size spectrometer	POPS, Handix (Fort Collins, CO, USA)	Particle number size distribution, D_P = 0.15–2.9 μm	5%		
Video Ice Particle Sampler, VIPS					
Video microscope		Liquid water and/or ice	10 m	Cloud flag	10 m
Cloudnet					
Microwave radiometer	Hatpro, RPG (Meckenheim, DE)			Liquid water path, LWP	20 g m^{-2}
+ Cloud radar	KAZR, ProSensing (Amherst, MA, USA)			Ice water path, IWP	40%
				Ice water content, IWC	−30% to +40%
+ Lidar	PollyXT, TROPOS (Leipzig, Germany)			Liquid water content, LWC	15%–25%

TIR = thermal-infrared radiation.

particle images. The observations were used to indicate the presence of liquid water or ice, for particles of just a few microns and above.

BELUGA was operated during Leg 4 (June 19–July 31, 2020) of MOSAiC. It was deployed at the "New Balloon Town" site (Shupe et al., 2022), 260 m away from the

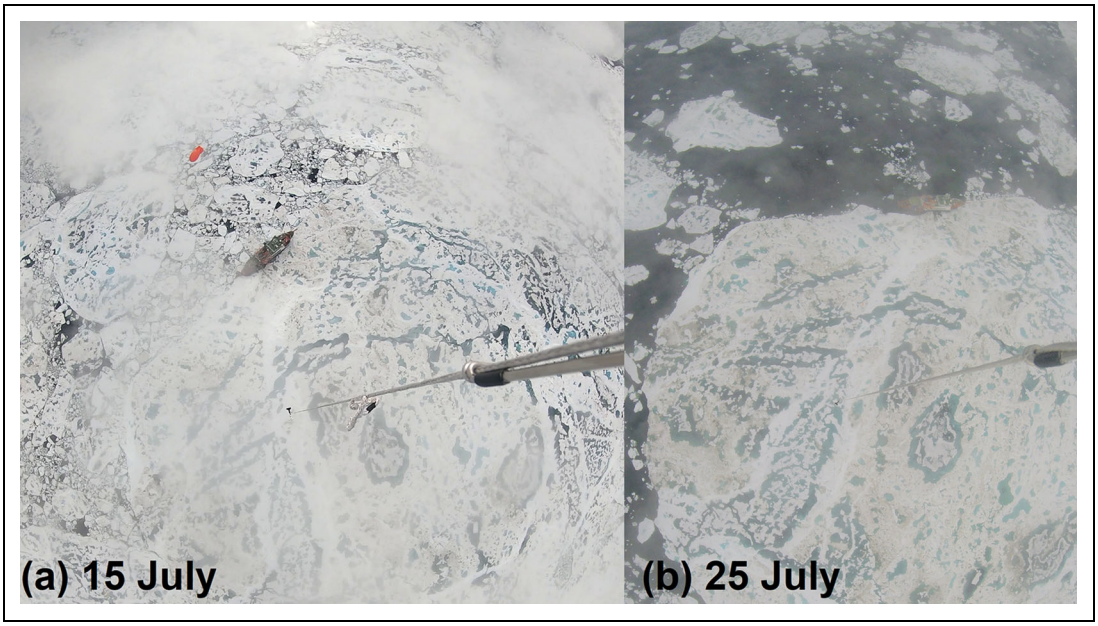

Figure 1. The Multidisciplinary drifting Observatory for the Study of Arctic Climate ice floe. The ice floe as seen from a downward-looking camera installed on BELUGA at about 600 m above ground on (a) July 15 and (b) July 25, 2020. The floe was located approximately at 81.3 N, 0.3 E and 79.9 N, 0.9 W, respectively. BELUGA = Balloon-bornE moduLar Utility for profilinG the lower Atmosphere.

starboard side of the research vessel (RV) Polarstern (Knust, 2017). BELUGA was operational between June 29 and July 29, 2020. During this period, the ice floe on which the MOSAiC ice camp was established drifted from the Arctic ocean (81.8 N, 9.2 E) to the Greenland Sea (79.6 N, 2.2 W). BELUGA flights were performed on 14 different days, with a total of 33 flights up to an average altitude of 970 m and a maximum of 1,500 m. The typical ascent and descent rate was 0.5–1 m s^{-1}. Methods for the derivation of in situ dissipation rates, turbulent energy fluxes, and radiative heating rates profiles from BELUGA data are given by Egerer et al. (2019). Radiative transfer model (RTM) simulations and back-trajectory simulations were used to complement the analysis of the observations. Observations from a 10-m meteorological tower located at Met City (Cox et al., 2021b) and the nearby Atmospheric Surface Flux Station (Cox et al., 2021a), both within a couple hundred meters of the balloon operations, were used as surface references.

3. Meteorological conditions and clouds

Here, we introduce the general meteorological conditions of the balloon operation period, with a focus on 3 selected days (July 13, 23, and 24, 2020). The Balloon Town site of the summer MOSAiC ice camp was established on June 29, 2020, during the melting period. **Figure 1** shows 2 photographs of the ice floe, on July 15 and 25, 2020, which illustrate the change of surface conditions during the BELUGA observational period. Over time, the snow melted, melt ponds grew, the ice itself became thinner, and the local sea ice concentration decreased.

Radiosondes were regularly launched from RV Polarstern with 6 hourly intervals (Maturilli et al., 2021). Reanalyses with the ECMWF Reanalysis 5th Generation data set (ERA5, Hersbach et al., 2020) indicate that July 2020 mean conditions at the MOSAiC location were the warmest and wettest of the period 1979–2019 (Rinke et al., 2021). **Figure 2** shows the temporal evolution of air temperature and mean wind speed and direction in the lower troposphere derived from radiosonde data. Here, the extraordinary warm and wet conditions identified by Rinke et al. (2021) are illustrated: Above a surface layer with temperatures around the freezing/melting point, there is often a thick warm layer extending up to 2–2.5 km height.

Five synoptically different periods (I–V) were identified on the basis of **Figure 2**. **Figure 3** presents the corresponding maps of geopotential height, wind vector, and potential temperature averaged over the five selected periods. These results are calculated from ERA5 reanalysis data.

During period I (June 29–July 4), a low-pressure system located over Northern Norway caused an easterly flow advecting warm air toward the ice camp. On its way, this air mass significantly cooled as indicated by the still low temperatures measured in all altitudes (**Figure 3a**). During phase II (July 5–11), a series of low-pressure systems, which was linked to the dominant low-pressure system close to Iceland, crossed the ice camp of MOSAiC. Strong easterly winds advected a warm air mass in the free troposphere above the surface inversion. Strong surface winds inhibited balloon operations (**Figure 3b**). During phase III (July 12–14), cold and calm conditions prevailed, caused by a high-pressure system located over the North Pole (**Figure 3c**). Frequently changing temperature and wind conditions characterized period IV (July 15–24). Weak low-pressure systems passed the ice camp leading to low gradients in the averaged geopotential height

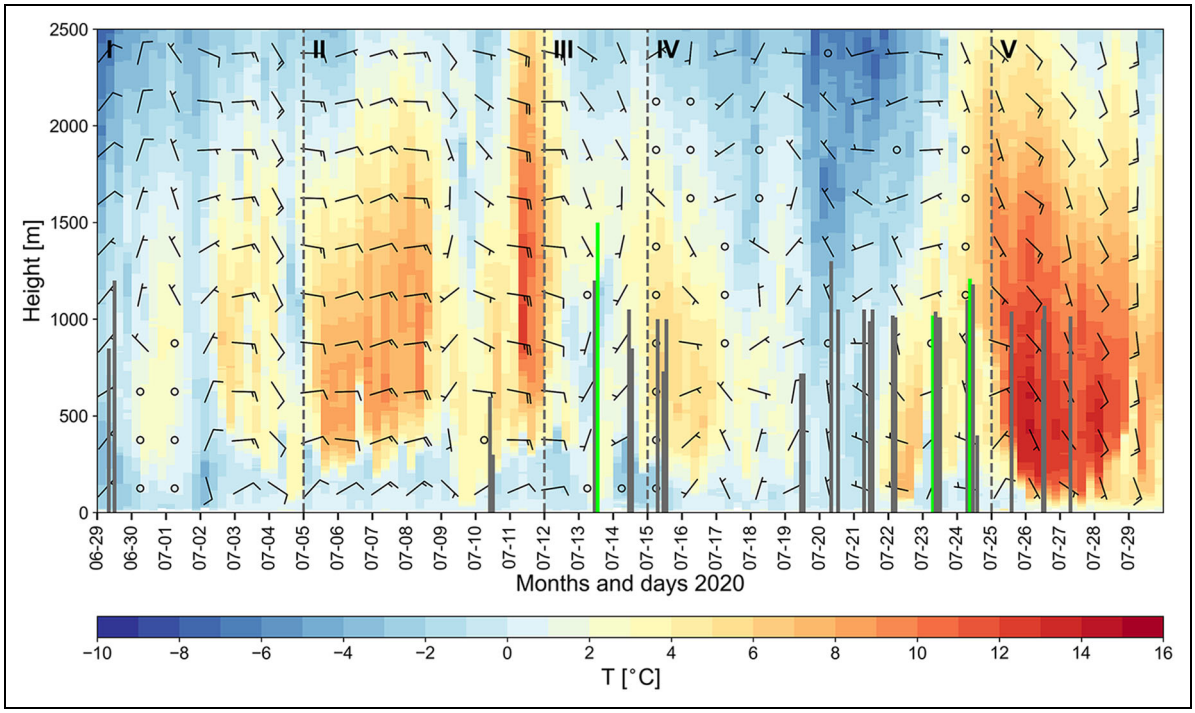

Figure 2. Time series of local conditions above research vessel (RV) Polarstern. Temperature and wind field from radiosondes launched at RV Polarstern during BELUGA deployment period (June 29–July 29, 2020). BELUGA flights are marked by vertical lines and show the maximum height reached. Core flights presented in the case study are highlighted in green. BELUGA = Balloon-bornE moduLar Utility for profilinG the lower Atmosphere.

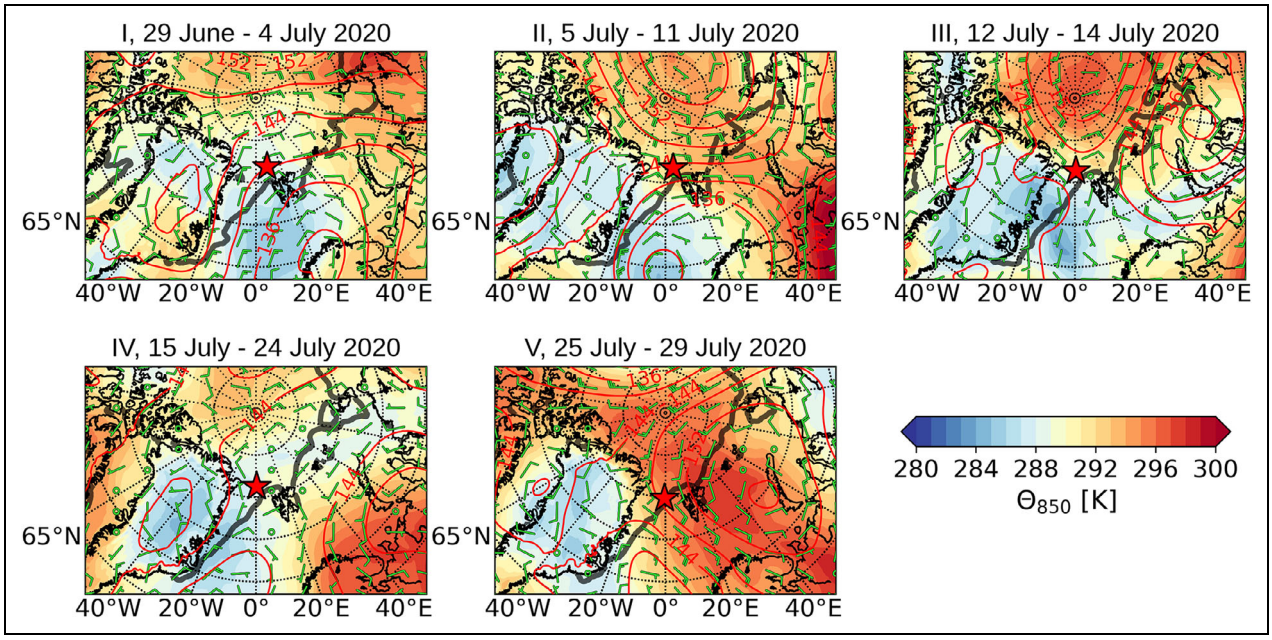

Figure 3. Synoptic periods. Contours of geopotential height labeled in decameter (red), wind vectors (green barbed arrows), and potential temperature (color scale) at 850 hPa. Hourly ERA5 data were averaged for the synoptic periods I–V. The ice edge is marked with a gray line.

maps. Still, a weak average northwesterly wind was observed (**Figure 3d**). This wind advected cold air and lowered the height of the first temperature inversion. A strong persistent high-pressure system over the Barents Sea dominated period V (July 25–29). A significant intrusion of warm and moist air approached from the southeast (**Figure 3e**). During that period, the air temperature reached a maximum of 14°C at about 300 m height.

In **Figure 4**, cloud type, profiles of liquid and ice water contents (LWC and IWC) and the liquid water path (LWP) retrieved from ground-based remote sensing are plotted as measured during the BELUGA deployment period up to

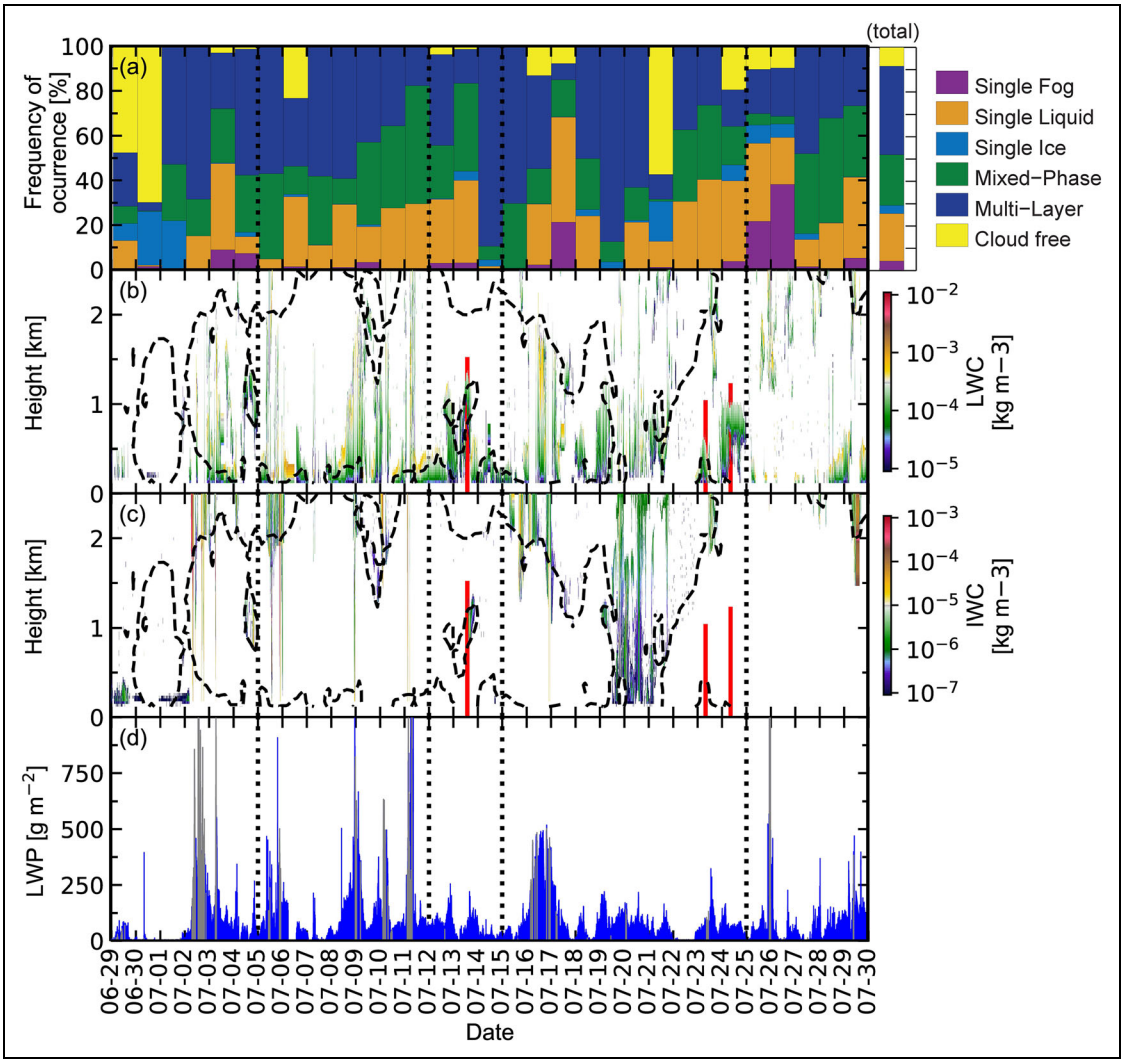

Figure 4. Cloudnet time series. Time-height series of (a) cloud type occurrence, (b) liquid water content, (c) ice water content, and (d) liquid water path retrieved from synergistic ground-based remote sensing (Cloudnet) during the period of June 29–July 29, 2020. Vertical dotted lines separate the synoptic time periods (I–V). The black dashed lines in (b) and (c) indicate the 0° isotherm derived from the 6 hourly radio soundings. The red lines indicate the BELUGA flights. BELUGA = Balloon-bornE moduLar Utility for profilinG the lower Atmosphere.

2.5 km height. The cloud classification and cloud microphysical products were derived by applying the instrument synergy approach of Cloudnet (Illingworth et al., 2007), following Griesche et al. (2020). LWC and IWC are based on the vertically pointing Ka-band cloud radar reflectivity (KAZR). LWP was derived from microwave radiometer data. These derived cloud microphysical properties are used as inputs for computing atmospheric radiation profiles. Cloudnet revealed mostly cloudy conditions, with the majority of the clouds located below 2 km. A secondary maximum of cloud occurrence was roughly at 5 km height. Due to the high temperatures in the lower troposphere during most of the time, the amount of ice in the lower 2.5 km was limited. Only occasionally during period IV, between July 19 and 21, ice was present down to the surface, although in rather low amounts. The cloud top height of the respective ice-containing cloud layers in the lowest 2.5 km during these days, derived from the cloud radar observations, indicates that the ice particles must have formed at temperatures >−15°C (on July 19, 2020, even >−10°C). This indicates the presence of highly active ice nucleating particles in these low-level Arctic clouds, a phenomenon already observed, for example, in Griesche et al. (2021).

The LWP showed a median of 43 g m^{-2} reaching peak values up to 1,000 g m^{-2} during precipitation events. Periods of precipitation events reaching down to the surface are indicated in gray in **Figure 4d**. Under these conditions, the dome of the microwave radiometer might get wet and the respective values have to be handled with care. The average (median) reliable (i.e., filtered for precipitation events) values of the five periods were 60 (8), 103 (62), 50 (42), 79 (48), and 56 (36) g m^{-2}. Mean and median LWP were derived excluding precipitation events.

The total occurrence of single-layer liquid clouds observed during the analyzed period (20% of the time, **Figure 4**) was larger than for a comparable study

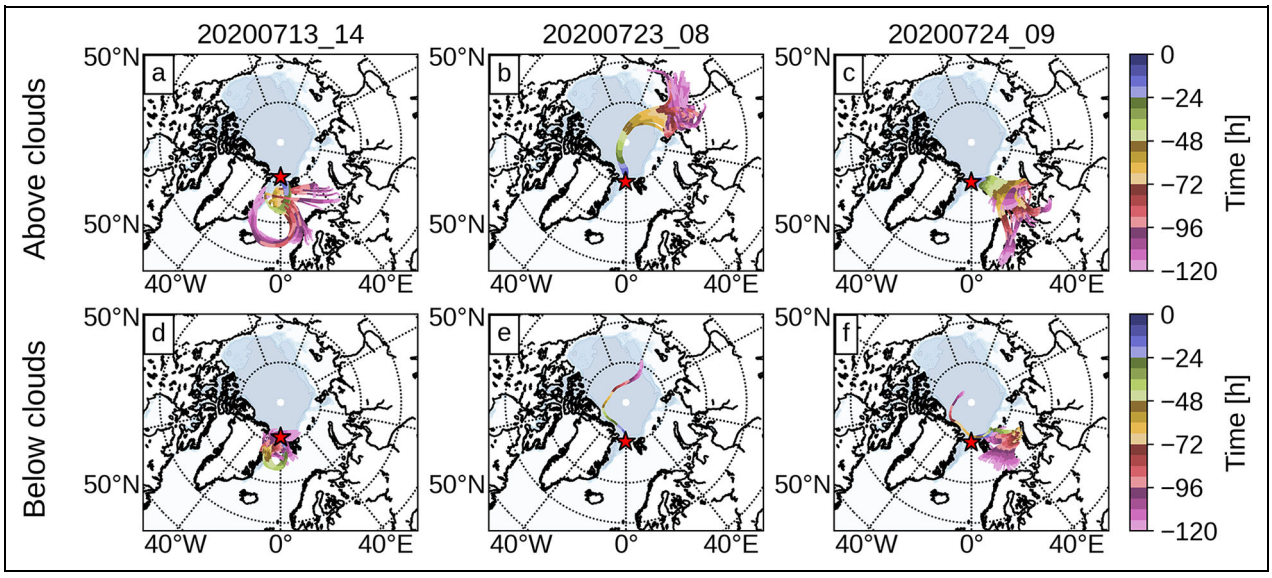

Figure 5. Kinematic back-trajectories. Trajectories of the air mass above and below the cloud cover on (a and d) July 13, (b and e) July 23, and (c and f) July 24, 2020, at selected coordinated universal time times. The sea ice extent for the time is included as a gray shaded area.

performed with data from the Polarstern cruise PS106 conducted in the Arctic ocean north and northeast of Svalbard in June and July 2017 (Griesche et al., 2020). During the entire PS106 campaign, single-layer liquid clouds were observed less than 5% of the time. This difference in liquid-only clouds was at the expense of single-layer ice and mixed-phase clouds, indicating that the BELUGA observational period was warmer than the one during PS106. Shupe (2011) provided an annual cycle of cloud phase fraction for the 3 Arctic sites Utqiagvik (formerly known as Barrow), SHEBA, and Eureka. In comparison to the July ice-only cloud fraction at these 3 sites (Utqiagvik: 40%, SHEBA: 45%, and Eureka: 40% monthly mean occurrence), considerably less pure ice clouds were observed during the investigated MOSAiC period (<5%, **Figure 4**). During the 3 investigated days, the liquid cloud fraction was larger than the average of the entire period (>35% of each day, **Figure 4**). The mixed-phase and ice cloud fractions differ on the 3 days. While on July 13 and 24, between 5% and 10% of the time ice clouds were detected, and no pure ice clouds were observed on July 23. The mixed-phase cloud fraction was largest on July 13 with 35%, on July 23, it was 30%, and on July 24, during less than 20% of the day, single-layer mixed-phase clouds were observed. However, most ice-containing clouds (ice-only and mixed-phase) on these days were located above 2-km altitude.

4. Cloud characteristics influenced by air mass origin: Three case studies

Three single-layer boundary-layer clouds capped by a temperature inversion (July 13, 23, and 24, 2020) were investigated in detail to illustrate the potential of the BELUGA observations. The analysis presented in this section aims to identify the influences of air mass characteristics on the cloud properties using BELUGA measurements.

4.1. Air mass trajectories

To identify air mass origins and pathways, 5-day back-trajectories were calculated using Lagranto (Sprenger and Wernli, 2015). The meteorological input required for these simulations was based on the ERA5 reanalysis data set (Hersbach et al., 2020), similar to the analysis recently performed by Silber and Shupe (2022) to investigate the origin of liquid-bearing clouds during the MOSAiC campaign. ERA5 was retrieved at 137 model levels and at 0.25° lateral resolution. Trajectories were initialized within a radius of 5 km around the position of RV Polarstern and with 2-km horizontal spacing. This yielded 21 trajectories for each altitude. Vertically, air mass trajectories were initiated every 10 hPa, beginning 10 hPa above ground and reaching 850 hPa (July 23 and 24) and 750 hPa (July 13), respectively. The vertical extent was increased for July 13 since the cloud top reached higher altitudes of 1,300 m.

On July 13, the air mass circled over the ice-covered region surrounding RV Polarstern, the marginal sea ice zone, and the ice-free ocean (**Figure 5a** and **d**). This holds for both the air above and below the cloud layer. The original Arctic air mass was recycled by the circulation and reentered the ice-covered Arctic. Therefore, this air mass is denoted as "aged Arctic" in the following. On July 23, the air mass originated in Siberia and then crossed the central Arctic sea ice (**Figure 5b** and **e**). This scenario is chosen as an example for an air mass "advected over sea ice." On July 24, the air mass was transported from Northern Europe over the Barents Sea, and partially over Svalbard, toward the location of MOSAiC (**Figure 5c** and **f**), eventually reaching it from the north. Having not crossed large distances over sea ice, this air mass is denoted as "advected over open ocean."

Overall, the cases on July 13 and 24 resemble typical (multilayer) liquid-bearing cloud systems advected over warmer oceans, while the genesis of the Arctic-originated liquid clouds observed during July 23 might

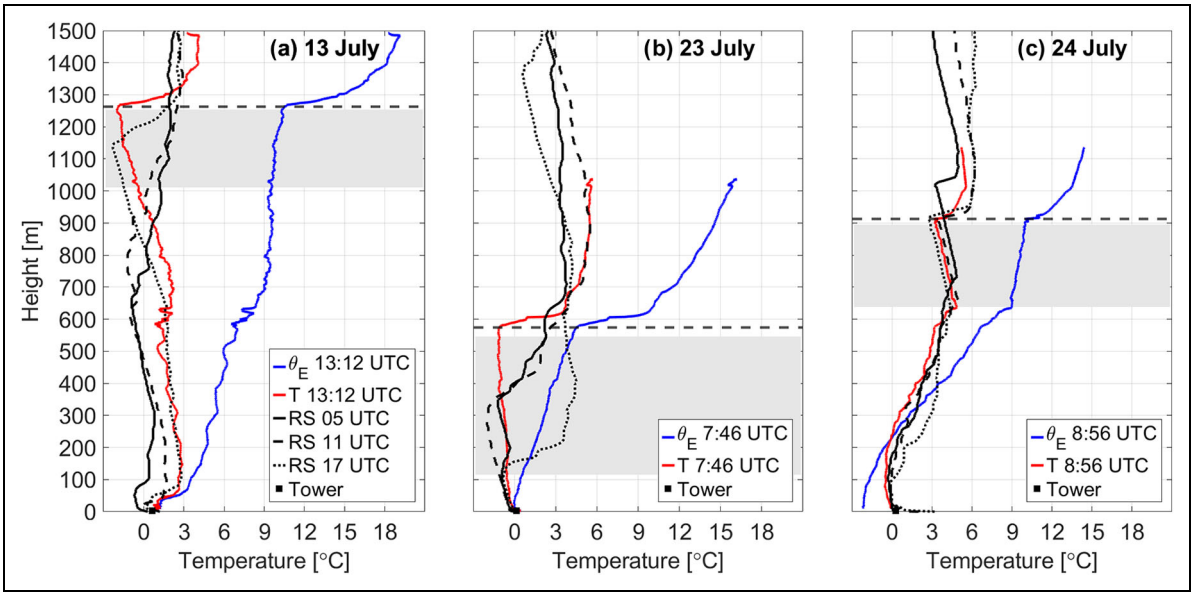

Figure 6. Temperature profiles. Profiles of equivalent potential temperature (blue lines) and temperature (red lines) from extended meteorological package. Profiles are also shown from radio soundings at 5, 11, and 17 coordinated universal time (black lines). The 2 m temperature from Met City Tower is indicated by a square. The main inversion is marked as a horizontal dashed line. Cloud boundaries estimated from broadband irradiances of the broadband radiation package are indicated as gray shaded areas.

be through persistent radiative cooling of elevated air masses (Silber and Shupe, 2022).

4.2. Air temperature profiles and clouds

To characterize the stratification of the atmospheric columns probed by BELUGA, vertical profiles of air temperature are presented in **Figure 6**. These standard meteorological data were measured by the EP and also provided by the regular radiosondes. The temperature profiles measured by BELUGA and the nearest-in-time radiosondes matched reasonably but also suggest some spatiotemporal variability. This observed variability demonstrates the value of having different temperature sensors distributed on the BELUGA payloads, which provide measurements directly comparable to the other observations rather than relying fully on proximal radiosonde profiles.

The ABL was topped by a distinct temperature inversion on each analyzed case. On July 13, the base of the main inversion (6 K) was observed at 1,262 m altitude, on July 23, the base height of the inversion (6 K) was located at 575 m, and on July 24, the inversion (2 K) base height was located at 913 m. Weaker secondary inversions were identified on July 13 and 24, which delineate the base of cloud-driven mixed layers. Temperature profiles of the three air masses match with the idealized structures presented by Tjernström et al. (2019) and Schmale et al. (2021). On July 13 and 23, the observations are representative of Arctic air masses, while measurements from July 24 indicate a warm advected air mass that was still gradually cooling, in agreement with simulations by back-trajectories.

Thermodynamic coupling was defined using vertical variations of the equivalent potential temperature θ_E similar to Sotiropoulou et al. (2014). The profile of equivalent potential temperature θ_E clearly suggests that the cloud is decoupled from the surface for July 13, with a clear transition from the surface layer to the cloud-driven mixed layer at about 600 m. On July 23, a weak difference of $\Delta\theta_E \asymp 0.5$ K between surface and cloud base is on the edge for the definition of the layer as decoupled. However, the large increase in θ_E within the cloud suggests that the layer is not well mixed. On the next day, the layer connected to the surface (below 600 m) exhibits instead a strong gradient of θ_E, indicating a cloud layer decoupled from the surface.

Cloud properties retrieved from ground-based remote sensing techniques employing the Cloudnet algorithm are presented in **Figure 7**. Cloud boundaries defined using the in situ microphysical observations by Video Ice Particle Sampler (VIPS) and broadband irradiances by BP are additionally plotted. Differences on the order of tens of meters are caused by measurement uncertainties, instrument sensitivity limits, cloud heterogeneity (spatial and temporal), and the thickness of the layers (30 m) used in the retrievals by Cloudnet. The retrieval results show single-layer liquid clouds in all cases located underneath the main temperature inversion, in agreement with the cloud top heights estimated from the broadband irradiances (**Figure 6**). There were no indications of ice in any of the three clouds.

In situ cloud microphysics profiles by VIPS were obtained on July 13 and 24. Cloud particles were recorded at heights between 1,093 and 1,277 m on July 13 and between 534 and 899 m on July 24 (**Figure 7a**, vertical lines). All cloud particles were liquid, which confirms the classification by Cloudnet.

The average LWP retrieved by the Cloudnet algorithm varied over the profiling time of BELUGA. On July 13, the

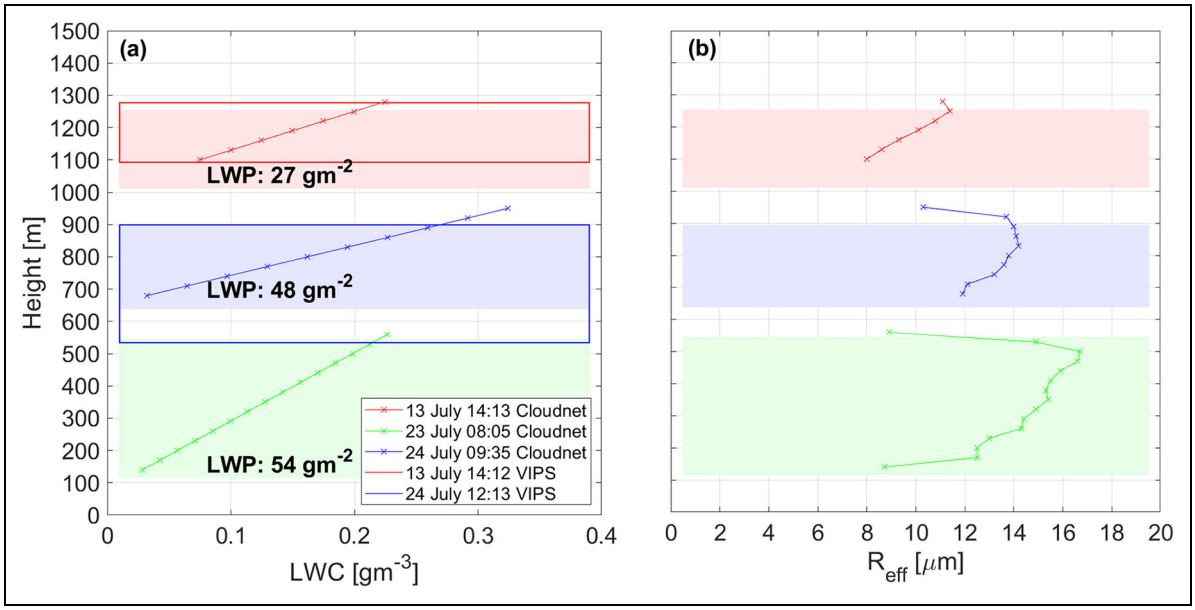

Figure 7. Cloud (a) liquid water content (LWC) and (b) particle effective radius R_{eff}. Profiles of (a) LWC and (b) particle effective radius (R_{eff}) derived from Cloudnet for July 13 (red), July 23 (green), and July 24, 2020 (blue). Shaded rectangles indicate the cloud cover derived from the broadband radiation package, and the empty rectangles the cloud cover indicated by Video Ice Particle Sampler (VIPS). Liquid water paths by Cloudnet are displayed as text. Note that VIPS data on July 24 are not from the same flight, while no VIPS data are available for July 23.

LWP during BELUGA profiles ranged between 18 and 49 g m^{-2} with a mean value of 27 g m^{-2}. On July 23 and 24, values ranged between 47 and 99 g m^{-2} and 36 and 61 g m^{-2}, with respective averages of 54 g m^{-2} and 48 g m^{-2}. These values are in the range of the median LWP of 43 g m^{-2} observed by Cloudnet during the 4-week BELUGA measurement period.

Cloudnet provides estimates of LWC and particle effective radius (R_{eff}) profiles using the assumption of adiabatic clouds. It is known that entrainment processes at cloud top reduce LWC and R_{eff} in the uppermost part of cloud layers, and thus, the adiabatic assumption is questionable. During subadiabatic conditions, the resulting overestimation of LWC at cloud top could influences the radiative properties derived from these cloud profiles.

4.3. Broadband irradiance profiles and derived heating rates

Profiles of net irradiances (*Fnet*) and radiative heating rates (ζ) were calculated from BP measurements and compared to radiative transfer simulations using the libRadtran 2.0.3 software package (Emde et al., 2016).

The radiative transfer equation solver twostr (Kylling et al., 1995) was used and initialized with profiles of air pressure, air temperature, air density, and concentrations of ozone, oxygen, water vapor, carbon dioxide, and nitrogen dioxide from the Sub-Arctic standard atmosphere defined by Anderson et al. (1986). The predefined atmosphere is used to calculate molecular absorption and Rayleigh scattering of the atmospheric gases. Clouds and aerosol particles were defined separately. The nearest-in-time radiosonde temperature and water vapor profiles were used (typically measured less than 3 h before or after a given time). The surface albedo assumed for each simulation ($\alpha = 0.44$) was derived from drone observations at 50 m (Calmer et al., 2021) and represents all of the variability contained in a surface area of approximately 200 m diameter around the observation site. Profiles of LWC and droplet effective radii (R_{eff}) for water droplets retrieved from Cloudnet were used as an input for the radiative transfer simulations with a 30-m vertical resolution.

The cloud radiative effect on profiles of net TIR irradiance is illustrated in **Figure 8** for the 3 cloud cases investigated here. All profiles feature strong vertical gradients close to cloud top, with large negative net irradiances (indicating a significant irradiance divergence) of about –80 to –60 Wm^{-2}. The ground-based irradiance measurements (black squares in **Figure 8**) match within instrument uncertainties with the BELUGA observations in the first 10-m altitude. A vertical displacement, up to 60 m, between the measured and the simulated irradiance profiles was observed. These differences are attributed to the uncertainty of the cloud top altitude estimated by Cloudnet and the rather coarse vertical resolution of Cloudnet (30 m).

Downward and upward solar irradiance profiles are shown in **Figure 9**. The solar irradiance (**Figure 9**, colored solid lines) is influenced by the solar zenith angle, which prevents comparing absolute values between the 3 cases characterized by varying solar zenith angles. Furthermore, there are temporal and spatial inhomogeneities of cloud cover, which display in the vertical profiling due to the slow ascent and descent rates of about 0.5–1 m s^{-1}. Such inhomogeneity effects are not covered by the one-dimensional radiative transfer simulations (**Figure 9**, dashed lines), showing smooth profiles, with net solar

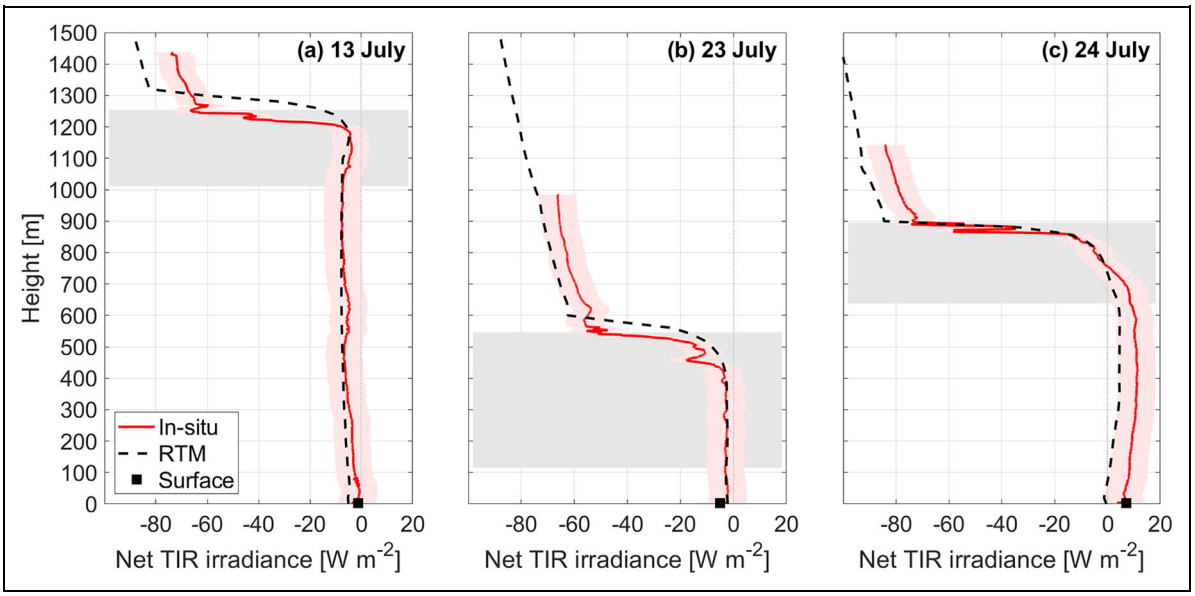

Figure 8. Profiles of net thermal-infrared radiation (TIR) irradiances. Measured (solid lines) and simulated (dashed lines) net TIR irradiances for (a) July 13, (b) July 23, and (c) July 24, 2020. A square marks the surface measurement from the Atmospheric Surface Flux Station. The height range of the clouds as derived from the broadband radiation package is shown by the gray area. The measurement uncertainty is indicated by a red-shaded band along the measured net irradiance.

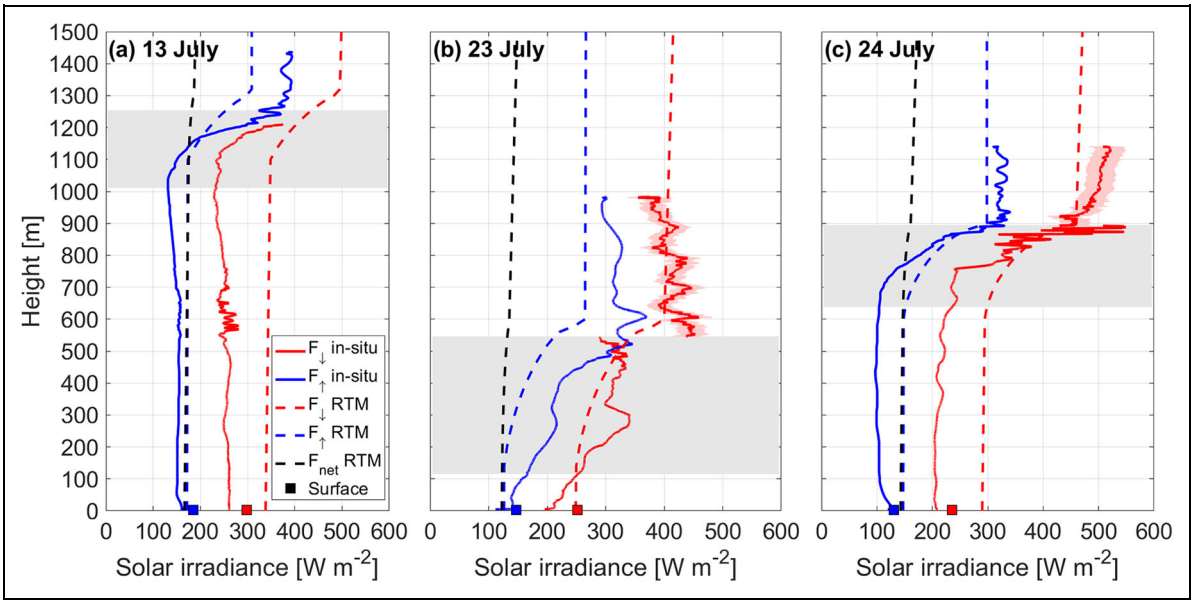

Figure 9. Profiles of solar irradiances. Attitude corrected observed (lines) and simulated (dashed lines) solar irradiances for (a) July 13, (b) July 23, and (c) July 24, 2020. Downward irradiances are colored in red, upward irradiances in blue, and the simulated net solar irradiance is shown in black. A square marks the surface measurement from the Atmospheric Surface Flux Station. The height range of the clouds as derived from the broadband radiation package is shown by the gray area. The 5% measurement uncertainty for the downward solar irradiance above clouds is indicated by a red-shaded band along the measured values. The 2% uncertainty for the downward solar irradiance below clouds, and for the upward solar irradiance, is not shown.

irradiances (**Figure 9**, dashed black line) on the order of 100 Wm^{-2} at the surface, slightly increasing within and above the cloud. The use of a fixed value for the surface albedo in the RTM introduces an underestimation in the upward solar irradiance for the lowermost 100 m of the profile. The discrepancy is explained by a gradually increasing field of view, depending on height, which eventually takes into account the larger presence of melt ponds and open water in the broader spatial scale, as displayed in **Figure 1**. Solar irradiances are also influenced

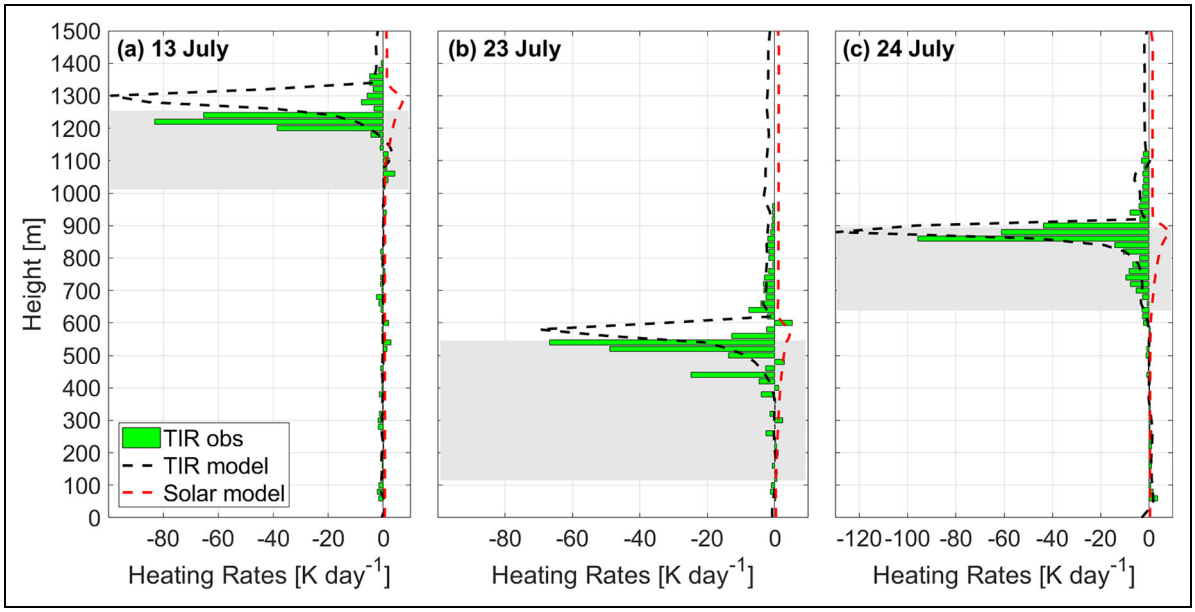

Figure 10. Profiles of radiative heating rates. Measured (20 m averages histograms) and simulated (dashed black lines) thermal-infrared radiation (TIR) heating rates and simulated (dashed red lines) solar heating rates for (a) July 13, (b) July 23, and (c) July 24, 2020. The uncertainty for the measured TIR heating rates is ± 12 K day^{-1}. The height range of the clouds as derived from the broadband radiation package BP is shown by the gray area.

by the attitude of the instrument. The leveling mechanism on BP compensates only partially the change in the tether's inclination, and therefore, a postcorrection is applied following Bannehr and Schwiesow (1993). However, the correction can only partly consider strong deviations from the horizontal reference plane. Therefore, the remaining offsets by the tilt of BP induce fluctuations in the measured values of solar irradiance.

Solar and TIR net irradiances have been converted into atmospheric heating rates similar to Egerer et al. (2019). The derived TIR cooling and solar heating (**Figure 10**) are particularly strong in the cloud top region for all three cases.

Observed TIR cooling (**Figure 10**) is larger in magnitude than 65 K day^{-1} and dominates over the modeled solar heating, which never exceeded 10 K day^{-1}. The simulated values of the TIR cooling exhibit larger values than the measurements, in particular close to the cloud top possibly due to an overestimation of LWC by Cloudnet in this region. Differences might also arise from spatial gradients, the 30-m vertical resolution of the remote sensing retrievals, and uncertainty in the retrievals.

Cloud microphysical and temperature profiles modulate the TIR cooling at cloud top. Larger LWC supported by warm cloud tops exhibits stronger cooling (July 24). Cloud top cooling transfers to the cloud layer via turbulent mixing. A very simplified approximation of the total (TIR and solar) radiative effect of the cloud-driven mixed layer can be made by assuming that the cloud-driven cooling will be mixed over the full layer. This radiative effect would cool the cloud-driven mixed layer at 600–900 m by about 11 K day^{-1} on July 24. The layer cooling for the Arctic air masses of July 13 and 23 would be lower, about 4 K day^{-1}. The air mass is likely impacted by other processes, including the expected turbulent entrainment, that could modify the net cooling. Despite the large uncertainty related to this basic scheme, it can be hypothesized that the warm air mass advected over the open ocean undergoes a strong cooling during its transition within the Arctic. Such a strong radiative effect would modify the temperature profiles of the rather warm oceanic air mass, as seen in **Figure 6c**, within 12–24 h of interaction with the sea ice, in agreement with the transport time described by the back-trajectories for this case.

Despite the generalized cooling in the cloud-driven mixed layer for all the air masses, a significant distinction can be made about the observed heating rates at cloud base height (**Figure 10**). The air mass origin has an influence on the heat exchange between cloud base and the surface due to the temperature gradient. On July 13, cloud base warms with a rate of 5 K day^{-1}, while an opposite trend of –2 K day^{-1} is observed on July 24. No significant heating is observed on July 23. In the aged Arctic air mass case, TIR heating at cloud base is induced by a warmer surface and enhanced by a solar component. In the case of an air mass advected over the ocean, TIR cooling occurs at cloud base and is partially balanced by a weak solar warming. For the coupled cloud layer of the air mass advected over the sea ice, the cold cloud base is already in balance with the surface.

Overall, the cloud–surface radiative interactions depend on the air mass, in particular the vertical temperature profile. When the air mass and cloud are colder than the surface, the cloud base is radiatively warmed, while the cloud base is radiatively cooled when the air mass and cloud are warmer than the surface. The cloud in the "aged Arctic" air mass warms at its base, while in the "advected over open ocean" case, the cloudy air mass aloft is much

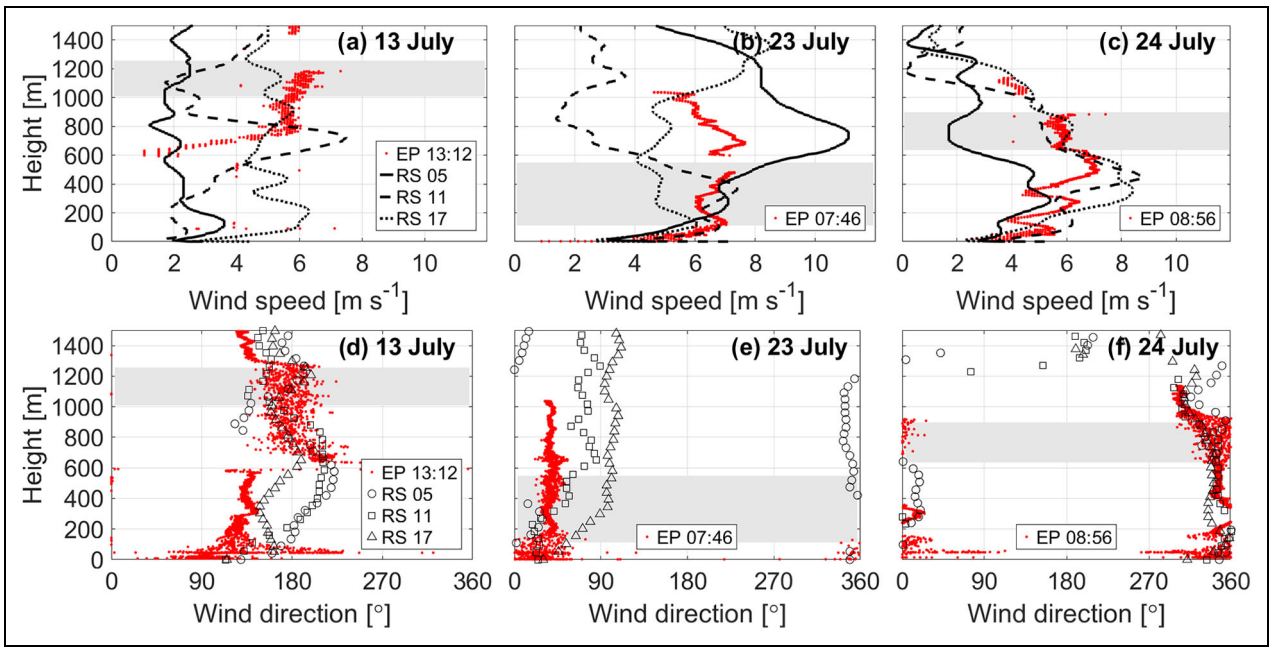

Figure 11. Profiles of wind speed and direction. Wind speed (a–c) and direction (d–f) on July 13, 23, and 24, 2020. All times are in coordinated universal time. Due to data gaps, measurements shown for July 13 are a combination of ascent and descent. The height range of the clouds as derived from the broadband radiation package is shown by the gray area. The absolute errors for wind speed and direction are 0.5 m s^{-1} and 5°, respectively.

warmer than the surface, such that this cooling at both cloud top and base serves to push the cloud more rapidly toward radiative equilibrium with the ice-covered surface.

4.4. Wind and turbulence

In situ profiles of horizontal wind speed and direction measured by EP are presented in **Figure 11**. Sections of the profile that were affected by icing of the Pitot tube were manually removed. Overall, the observations match with the boundary layer structures identified by the temperature profiles, and the mean wind directions support the flows indicated by synoptic and reanalysis maps.

On July 13, the decoupled layer between 600 and 1,300 m can be identified in the wind profiles (**Figure 11a** and **d**). The directional, and wind speed, shear at 600–700 m is possibly the primary cause of the decoupling between the cloud layer and the surface during this case.

On July 23, a 150-m surface-based layer with gradually height-increasing wind velocity lies under the cloud layer (**Figure 11b**). A low-level jet (LLJ) greater than 10 m s^{-1} is identified by the radio soundings, apparently being located above the cloud layer at the time of the BELUGA profile.

On July 24, wind velocity is highly variable between the surface and the inversion base, with an LLJ peaking at about 500 m (**Figure 11c**). A distinct decrease in the speed at 600 m marks the boundary with the decoupled cloud-driven mixed layer above. Wind speed fluctuations up to 1 m s^{-1} suggest the presence of turbulence in the decoupled cloud layer at 600–900 m.

Profiles of energy dissipation rate ε are shown for July 13 and July 24 in **Figure 12** and indicate increased turbulence within the cloud layer and at the surface. Data for July 23 are available only for a later flight, after cloud conditions changed. To show a consistent picture, these data are not shown here. Since the mean noise level for the determination of the energy dissipation rate as estimated by Egerer et al. (2019) with 10^{-5} m^2 s^{-3} is a function of the mean wind, an additional quality criterion based on the slope of the observed structure function was used. Thus, values below the mean noise level are also valid in some cases.

For July 13 and 24, in-cloud turbulence is expected by radiative cooling at cloud top. Turbulence sharply decreases above cloud top, at the lower bound of the cloud-capping temperature inversions.

On July 13, ε inside the cloud reaches values in the order of 10^{-3} m^2 s^{-3}, with turbulence extending also in the layer with increased wind velocity below the cloud, representing a cloud-driven mixed layer. Turbulence due to friction is produced at the surface, while light wind shear at about 300 m produces some weaker turbulence at that height. In the stably stratified regions above and below, turbulence is suppressed.

A similar magnitude of in-cloud ε is found for July 24, but here the layer with increased turbulence coincides with the cloud boundaries. Turbulence due to wind shear is observed at about 300 m, where wind speed has a minimum and a change in wind direction occurs. Surface-induced turbulence is found with values up to 10^{-3} m^2 s^{-3}.

Measured values of in-cloud ε in the order of 10^{-3} m^2 s^{-3} are consistent with the observations (Egerer et al., 2019) and remote sensing retrievals (Shupe et al., 2013) for a single-layer cloud in similar regions of the Arctic. For both days, the turbulent layer is confined in the decoupled

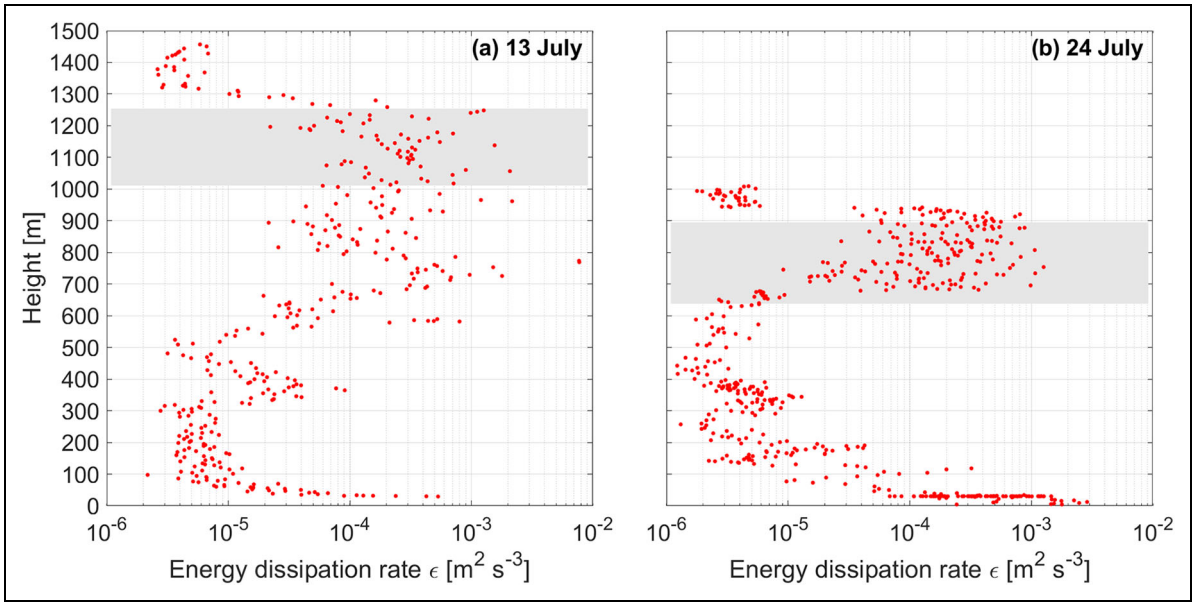

Figure 12. Profiles of energy dissipation rate. Energy dissipation rate ε on (a) July 13 and (b) July 24, 2020. The height range of the clouds as derived from the broadband radiation package is shown by the gray area.

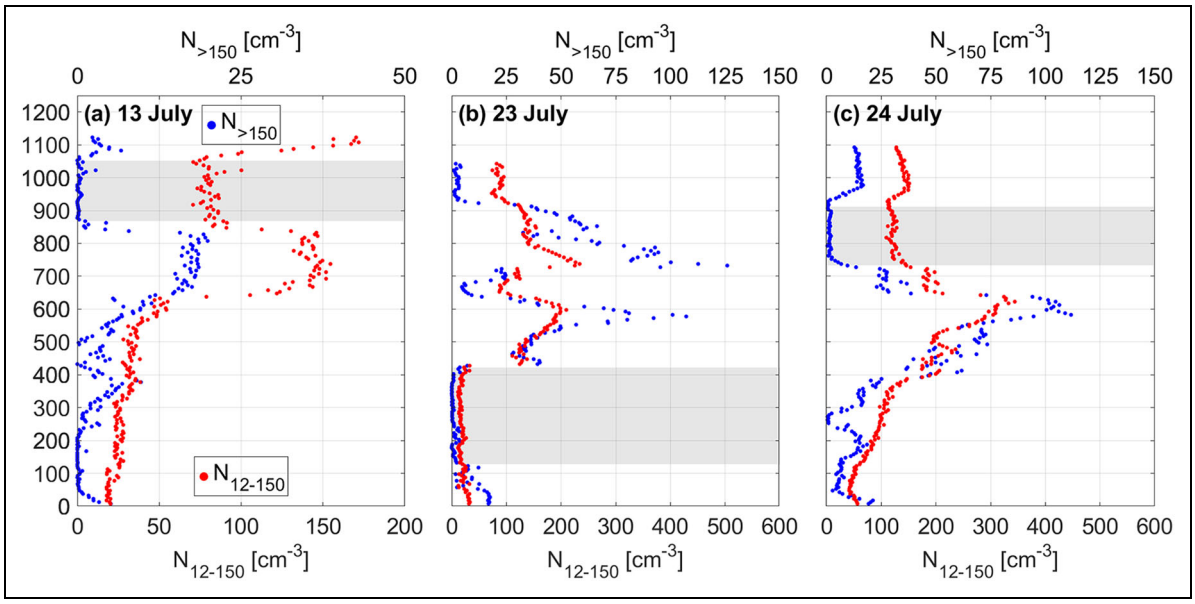

Figure 13. Profiles of aerosol particle number concentrations. Number concentration of particles in the diameter size range between 12 and 150 nm (N_{12-150}, red dots) and above 150 nm ($N_{>150}$, blue dots) measured on (a) July 13, (b) July 23, and (c) July 24, 2020. Observations were averaged over 5-m height steps with a resulting standard deviation of ±5%. Shaded areas indicate the cloud cover derived from ship-based remote sensing in combination with BELUGA in situ observations. BELUGA = Balloon-bornE moduLar Utility for profilinG the lower Atmosphere.

layer defined by the base of the primary (upper) inversion layer and approximately the top of the secondary (lower) inversion layer. The observed in-cloud turbulence driven by the TIR cooling results in an effective mixing of the cloud layer and possible entrainment of aerosol particles advected by the horizontal wind flow.

4.5. Aerosol particles

The vertical aerosol particle distributions on the 3 selected days shown in **Figure 13** reflect the boundary layer structure and the coupling state of the cloud (Shupe et al., 2013).

On July 13, particle number concentrations slightly increased up to the bottom of the decoupled cloud-driven mixed layer at about 620 m. A strong gradient in aerosol concentrations at that height indicates that the rather weak temperature inversion acted as a barrier for vertical particle exchange between the mixed layer and the air mass below. Some mixing seemed to occur at about 350 m due to the shear-induced turbulence. Turbulent

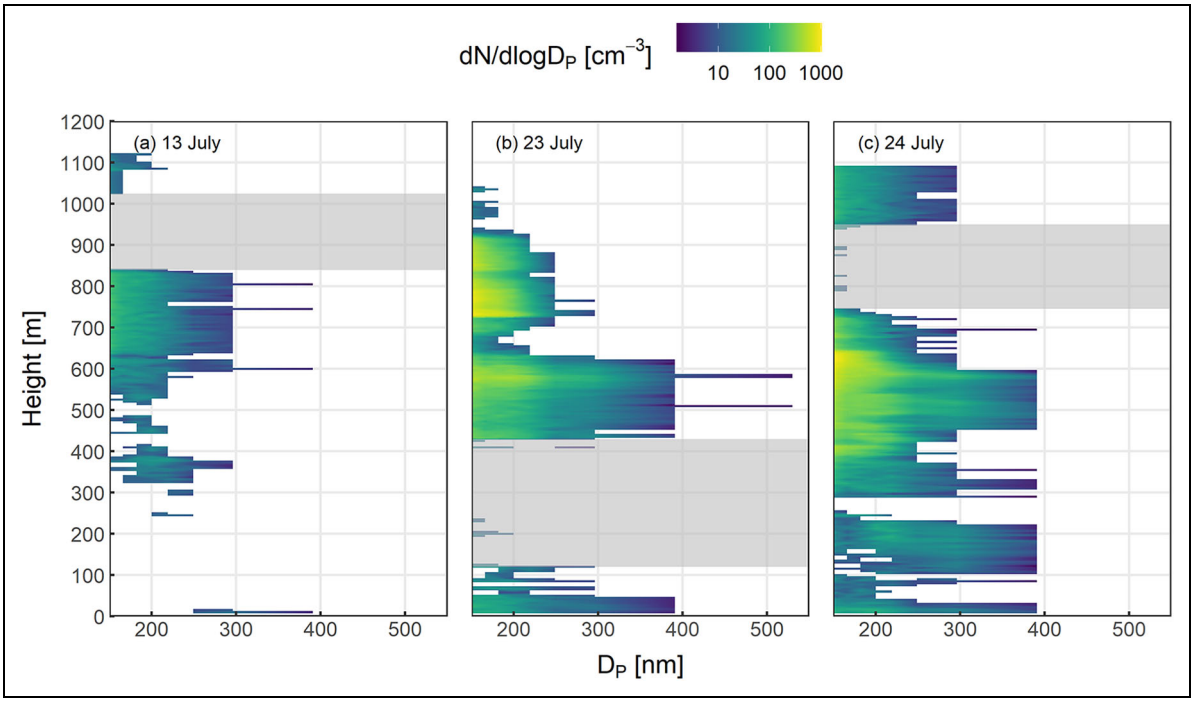

Figure 14. Profiles of particle number size distribution. Particle number size distributions were measured with an optical particle size spectrometer on (a) July 13, (b) July 23, and (c) July 24, 2020. A total of 14 bins covered a particle diameter range from 0.15 to 2.9 µm. Profiles are displayed as median distributions averaged over 5-m height steps. Gray shaded areas indicate the cloud cover derived from ship-based remote sensing in combination with BELUGA in situ observations. BELUGA = Balloon-bornE moduLar Utility for profilinG the lower Atmosphere.

mixing inside the cloud-driven mixed layer resulted in nearly constant particle concentrations between 620 m height and the cloud base, with most of the particles being activated into cloud droplets within the cloud layer. The observations indicate that all particles larger than 150 nm ($N_{>150}$) and about half of the particles between 12 and 150 nm (N_{12-150}) were activated into droplets. The strong temperature inversion at cloud top represented another barrier for vertical particle exchange, with slightly increased concentrations above the inversion, particularly for particles less than 150 nm in size.

On July 23, particle distributions indicate coupling of the cloud-mixed layer with the ground by rather constant N_{12-150} and $N_{>150}$ up to cloud base. A decrease of $N_{>150}$ to zero resulted from complete CCN activation inside the cloud. Two pronounced layers with about six times higher N_{12-150} and $N_{>150}$ than at the ground are a potential source of CCN by radiation-driven turbulent entrainment at cloud top. In that case, a share of 90% of N_{12-150} in the aerosol layer directly above the cloud were large enough to act as CCN.

The aerosol vertical structure in the transforming air mass on July 24 was more complex compared to the other two cases. The maximum N_{12-150} and $N_{>150}$ were observed inside an intermittent layer ranging from about 400–650 m height that coincided with the vertical extent of the LLJ observed in the wind profiles from the radiosondes and the EP. The weak temperature inversion at about 600 m decouples the particle layer from the cloud-mixed layer above, causing a strong gradient in aerosol concentrations. Given the main temperature inversion at cloud top and the lower particle concentrations aloft, CCN entrainment into the cloud probably occurred from below. In-cloud N_{12-150} indicates a 60% share of below cloud particles not being activated as CCN, while all particles larger than 150 nm served as seeds for cloud droplet formation.

Observed vertically resolved PNSDs (**Figure 14**) of accumulation mode particles between 150 and 550 nm in size show distinct differences on the 3 selected days. On July 23 and 24, the air masses carried significantly higher concentrations of particles above 300 nm than on July 13. Both near-surface PNSD on July 23 and 24 featured similar shapes to the PNSD of the particle layers centered at 500 m height yet with lower number concentrations. The two particle layers above the cloud on July 23 (**Figure 14b**) interestingly showed differently shaped PNSD. The upper layer was composed of smaller particles compared to the layer centered around 500 m height, while integrated number concentrations $N_{>150}$ were similar. The differently shaped PNSD of the two layers above the cloud on July 23 indicate either vertically varying particle source or particle processing while traveling in the free troposphere above the Arctic ABL.

Back-trajectory analysis showed that the particle layer below the cloud arriving with the air mass on July 13 (**Figure 5d**) traveled most of the time over the marginal ice zone (MIZ) and ice-free areas of the Greenland Sea with few anthropogenic particle sources. In contrast to that, the particle layers captured above the cloud on July 23 (**Figure 5b**) and below the cloud on July 24 (**Figure 5f**) originated above northern Siberia and crossed the Northern

Searoute as the main shipping line during transport (Schmale et al., 2018). The air masses arriving on July 23 mainly traveled over pack-ice and the MIZ, while the back-trajectories for July 24 show a transport mainly over the ice-free ocean.

On July 23 and 24, the peak $N_{>150}$ was about 6 times higher than on July 13. These significantly higher accumulation mode particle concentrations, the PNSD showing larger particle sizes, and anthropogenic particle sources in the air mass origin indicate a possible long-range transport of aerosols on July 23 and 24.

Near-surface $N_{>150}$ was six times lower on July 13 than on July 23 and 24, corresponding to the peak ratio of $N_{>150}$. The distinctly higher $N_{>150}$ suggests that the air mass origin is of more importance than the surface conditions over which the air masses traveled to near-surface $N_{>150}$. In particular, on July 23, the near-surface layer PNSD corresponding to a diluted PNSD of the particle layer at 500 m suggests a downward mixing of particles possibly promoted by cloud-induced turbulence that fosters vertical particle exchange across the strong temperature inversion. The layer with increased particle concentrations at 500 m on July 24 was probably originally extending down to the ocean surface and was lifted when the relatively warm advected air mass reached the colder surface layer above the sea ice. Ground-based measurements are certainly not representative of aerosol–cloud interactions in the cloud-mixed layer aloft on July 13.

5. Conclusions

To illustrate the potential of the BELUGA data set for further research in the future, 3 cases of profile measurements through Arctic boundary layers (July 13, 23, and 24, 2020) with liquid–water bearing single-layer clouds were analyzed. A back-trajectory analysis shows that the 3 cases are linked to different air masses: "aged Arctic," "advected over sea ice," and "advected over open ocean." In situ vertical profiles from balloon-borne instruments operated on BELUGA were combined with ground-based cloud remote sensing, radio soundings, and radiative transfer simulations.

The observed clouds were characterized by the values of LWP between 18 g m^{-2} and 99 g m^{-2}; they were located beneath a temperature inversion. Such conditions are representative of the scenarios encountered during the BELUGA deployment period, between June 29 and July 29, 2020, where the ABL was very often topped by a strong temperature inversion.

The 3 investigated cases show a strong radiative cooling in the uppermost 60 m thick region of cloud top driven by negative net TIR irradiances. The measured TIR cooling is consistent with simulations assuming liquid water clouds with an LWP of 30–60 g m^{-2} by Turner et al. (2018). The variability of the observed and simulated cooling rates at cloud top points to the importance of LWC and cloud top temperature. Differences in the heating rates measured at cloud base indicate the influence of cloud base height and the difference in temperature between the surface and cloud base. The full MOSAiC data set, including all BELUGA cases as well as other supporting observations, can be used to understand the relative roles of cloud top and base cooling rates for supporting cloud processes and transforming air mass properties.

The presence of clouds is associated with turbulence generated by the strong cloud top cooling. This can lead to a highly variable cloud top height, which is in the measurements conducted on July 13, 2020, where the cloud top seems to extend into the inversion layer. It was shown that turbulence could be constrained to the cloud (July 24) or could also continue in the underlying cloud-driven mixed layer (July 13) that is decoupled from the surface layer. Measured in-cloud energy dissipation rates on the order of 10^{-3} m^2 s^{-3} match with observations from other Arctic locations (Shupe et al., 2013; Egerer et al., 2019). This data set, together with numerical simulations, is suited to analyze the properties of the ABL and to address the question of how clouds modulate the near-surface ABL.

Different structures in the aerosol particle distributions were observed. Aerosol particles that can be potentially activated as cloud droplets were present above (July 23), within (July 13), and below (July 24) the cloud-driven mixed layer. Vertically resolved PNSD observations combined with back-trajectory analysis pointed toward varying accumulation mode particle sources. Therefore, the BELUGA in situ observations can be used to identify the vertical distributions of aerosol particles and investigate how important is advection in modifying such structures. An analysis of the BELUGA data set combined with cloud and aerosol resolving numerical models will be needed to explain how these scenarios evolve based on aerosol and moisture availability.

Data accessibility statement

Data from BELUGA (Balloon-bornE moduLar Utility for profilinG the lower Atmosphere) instrument packages are available on PANGAEA (Broadband radiation package: Lonardi et al. [2022c] and Lonardi et al. [2022b]; Ultrasonic anemometer package: Egerer et al. [2021]; Cubic Aerosol Measurement Platform: Pilz et al. [2022]; Video Ice Particle Sampler: Lonardi et al. [2022a]). The extended meteorological package data set is available as a supplement of this manuscript (Data S1–S3). Radio soundings data are available on PANGAEA (Maturilli et al., 2021). Met City Tower and Atmospheric Surface Flux Station data are available on the Arctic Data Center (Cox et al., 2021a; Cox et al., 2021b).

Supplemental files

The supplemental files for this article can be found as follows:

Data S1–S3. PDF

Acknowledgments

We gratefully acknowledge the funding by the Deutsche Forschungsgemeinschaft (German Research Foundation)—project number 268020496—TRR 172, within the Transregional Collaborative Research Center "ArctiC Amplification: Climate Relevant Atmospheric and SurfaCe

Processes, and Feedback Mechanisms (AC)³" in subproject A02.

Radiosonde data were obtained through a partnership between the leading Alfred Wegener Institute, the Atmospheric Radiation Measurement User Facility, a U.S. Department of Energy (DOE) facility managed by the Biological and Environmental Research Program, and the German Weather Service (DWD).

Cloud radar data were obtained from the Atmospheric Radiation Measurement User Facility, a U.S. DOE Office of Science User Facility Managed by the Biological and Environmental Research Program.

Surface meteorology and radiation measurements were obtained from the University of Colorado/NOAA flux team.

This work was carried out and data used in this article were produced as part of the international Multidisciplinary drifting Observatory for the Study of Arctic Climate (MOSAiC) with the tag MOSAiC20192020. We thank all persons involved in the expedition of the Research Vessel Polarstern during MOSAiC (AWI_PS122_00) as listed in Nixdorf et al. (2021).

The authors want to express their gratitude to all personnel present during Leg 4 of MOSAiC, and in particular to H. Deckelmann, J. Hofer, and A. Schulz, for the precious help received in the field.

Funding

This research has been supported by the Deutsche Forschungsgemeinschaft (grant no. 268020496—TRR 172), the U.S. National Science Foundation (OPP-1724551), and Department of Energy Atmospheric System Research Program (DE-SC0021341).

Competing interests

The authors have no competing interests, as defined by *Elementa*, that might be perceived to influence the research presented in this manuscript.

MDS is a guest editor for the Elementa Special Feature on Multidisciplinary drifting Observatory for the Study of Arctic Climate but was not involved in the editorial or review process for this article.

Author contributions

Contributed to conception and design: ML, CP, AE, MW.

Contributed to acquisition of data: ML, CP.

Contributed to analysis and interpretation of data: EA, AE, UE, HG, BK, ML, MDS, HS, CP, BW, MW.

Drafted and/or revised this article: All authors.

Approved the submitted version for publication: All authors.

References

Anderson, GP, **Clough, SA**, **Kneizys, F**, **Chetwynd, JH**, **Shettle, EP**. 1986. AFGL atmospheric constituent profiles (0.120 km). Air Force Geophysics Lab Hanscom AFB MA.

Bannehr, L, **Schwiesow, R.** 1993. A technique to account for the misalignment of pyranometers installed on aircraft. *Journal of Atmospheric & Oceanic Technology* **10**(5): 774–777. DOI: http://dx.doi.org/10.1175/1520-0426(1993)010<0774:ATTAFT>2.0.CO;2.

Bekryaev, RV, **Polyakov, IV**, **Alexeev, VA.** 2010. Role of polar amplification in long-term surface air temperature variations and modern arctic warming. *Journal of Climate* **23**(14): 3888–3906. DOI: http://dx.doi.org/10.1175/2010JCLI3297.1.

Box, JE, **Colgan, WT**, **Christensen, TR**, **Schmidt, NM**, **Lund, M**, **Parmentier, FJW**, **Brown, R**, **Bhatt, US**, **Euskirchen, ES**, **Romanovsky, VE**, **Walsh, JE**, **Overland, JE**, **Wang, M**, **Corell, RW**, **Meier, WN**, **Wouters, B**, **Mernild, S**, **Mård, J**, **Pawlak, J**, **Olsen, MS**. 2019. Key indicators of Arctic climate change: 1971–2017. *Environmental Research Letters* **14**(4): 045010. DOI: http://dx.doi.org/10.1088/1748-9326/aafc1b.

Calmer, R, **de Boer, G**, **Hamilton, J**, **Lawrence, D**, **Borenstein, S**, **Cox, C**, **Argrow, B**, **Cassano, J.** 2021. HELiX Uncrewed Aircraft System data from the Multidisciplinary drifting Observatory for the Study of Arctic Climate (MOSAiC) Campaign [dataset]. DOI: http://dx.doi.org/10.18739/A2GH9BB0Q; https://arcticdata.io/catalog/view/doi:10.18739/A22J6857H.

Ceppi, P, **Brient, F**, **Zelinka, MD**, **Hartmann, DL.** 2017. Cloud feedback mechanisms and their representation in global climate models. *Wiley Interdisciplinary Reviews: Climate Change* **8**(4): e465. DOI: http://dx.doi.org/10.1002/wcc.465.

Cohen, J, **Zhang, X**, **Francis, J**, **Jung, T**, **Kwok, R**, **Overland, J**, **Ballinger, TJ**, **Bhatt, US**, **Chen, HW**, **Coumou, D**, **Feldstein, S**, **Gu, H**, **Handorf, D**, **Henderson, G**, **Ionita, M**, **Kretschmer, M**, **Laliberte, F**, **Lee, S**, **Linderholm, HW**, **Maslowski, W**, **Peings, Y**, **Pfeiffer, K**, **Rigor, I**, **Semmler, T**, **Stroeve, J**, **Taylor, PC**, **Vavrus, S**, **Vihma, T**, **Wang, S**, **Wendisch, M**, **Wu, Y**, **Yoon, J**. 2020. Divergent consensuses on Arctic amplification influence on midlatitude severe winter weather. *Nature Climate Change* **10**: 20–29. DOI: http://dx.doi.org/10.1038/s41558-019-0662-y.

Cox, C, **Gallagher, M**, **Shupe, MD**, **Persson, O**, **Solomon, A**, **Ayers, T**, **Costa, D**, **Hutchings, J**, **Leach, J**, **Morris, S**, **Osborn, J**, **Pezoa, S**, **Uttal, T**. 2021. Atmospheric surface Flux Station #50 measurements (Level 1 Raw), Multidisciplinary drifting Observatory for the Study of Arctic Climate (MOSAiC), central Arctic, October 2019–September 2020 [dataset]. DOI: http://dx.doi.org/10.18739/A2445HD46.

Cox, C, **Gallagher, M**, **Shupe, MD**, **Persson, O**, **Solomon, A**, **Blomquist, B**, **Brooks, I**, **Costa, D**, **Gottas, D**, **Hutchings, J**, **Osborn, J**, **Morris, S**, **Preusser, A**, **Uttal, T**. 2021. 10-meter (m) meteorological flux tower measurements (Level 1 Raw), Multidisciplinary drifting Observatory for the Study of Arctic Climate (MOSAiC), central Arctic, October 2019–September 2020 [dataset]. DOI: http://dx.doi.org/10.18739/A2VM42Z5F.

Creamean, JM, **de Boer, G**, **Telg, H**, **Mei, F**, **Dexheimer, D**, **Shupe, MD**, **Solomon, A**, **McComiskey, A.** 2021.

Assessing the vertical structure of Arctic aerosols using balloon-borne measurements. *Atmospheric Chemistry and Physics* **21**(3): 1737–1757. DOI: http://dx.doi.org/10.5194/acp-21-1737-2021.

de Boer, G, **Ivey, M**, **Schmid, B**, **Lawrence, D**, **Dexheimer, D**, **Mei, F**, **Hubbe, J**, **Bendure, A**, **Hardesty, J**, **Shupe, MD**, **McComiskey, A**, **Telg, H**, **Schmitt, C**, **Matrosov, SY**, **Brooks, I**, **Creamean, J**, **Solomon, A**, **Turner, DD**, **Williams, C**, **Maahn, M**, **Argrow, B**, **Palo, S**, **Long, CN**, **Gao, RS**, **Mather, J.** 2018. A bird's-eye view: Development of an operational ARM unmanned aerial capability for atmospheric research in arctic Alaska. *Bulletin of the American Meteorological Society* **99**(6): 1197–1212. DOI: http://dx.doi.org/10.1175/BAMS-D-17-0156.1.

Dexheimer, D, **Airey, M**, **Roesler, E**, **Longbottom, C**, **Nicoll, K**, **Kneifel, S**, **Mei, F**, **Giles Harrison, R**, **Marlton, G**, **Williams, PD.** 2019. Evaluation of ARM tethered-balloon system instrumentation for supercooled liquid water and distributed temperature sensing in mixed-phase Arctic clouds. *Atmospheric Measurement Techniques* **12**(12): 6845–6864. DOI: http://dx.doi.org/doi:10.5194/amt-12-6845-2019.

Egerer, U, **Ehrlich, A**, **Gottschalk, M**, **Griesche, H**, **Neggers, RA**, **Siebert, H**, **Wendisch, M.** 2021. Case study of a humidity layer above Arctic stratocumulus and potential turbulent coupling with the cloud top. *Atmospheric Chemistry and Physics* **21**(8): 6347–6364. DOI: http://dx.doi.org/10.5194/acp-21-6347-2021.

Egerer, U, **Gottschalk, M**, **Siebert, H**, **Ehrlich, A**, **Wendisch, M**. 2019. The new BELUGA setup for collocated turbulence and radiation measurements using a tethered balloon: First applications in the cloudy Arctic boundary layer. *Atmospheric Measurement Techniques* **12**(7): 4019–4038. DOI: http://dx.doi.org/10.5194/amt-12-4019-2019.

Egerer, U, **Pilz, C**, **Lonardi, M**, **Siebert, H**, **Wendisch, M.** 2021. Tethered balloon-borne measurements of turbulence during MOSAiC leg 4 in July 2020 [dataset]. DOI: http://dx.doi.org/10.1594/PANGAEA.931404; https://doi.pangaea.de/10.1594/PANGAEA.931404.

Emde, C, **Buras-Schnell, R**, **Kylling, A**, **Mayer, B**, **Gasteiger, J**, **Hamann, U**, **Kylling, J**, **Richter, B**, **Pause, C**, **Dowling, T**, **Bugliaro, L**. 2016. The libRadtran software package for radiative transfer calculations (version 2.0.1). *Geoscientific Model Development* **9**(5): 1647–1672. DOI: http://dx.doi.org/10.5194/gmd-9-1647-2016.

Ferrero, L, **Ritter, C**, **Cappelletti, D**, **Moroni, B**, **Mocnik, G**, **Mazzola, M**, **Lupi, A**, **Becagli, S**, **Traversi, R**, **Cataldi, M**, **Neuber, R**, **Vitale, V**, **Bolzacchini, E.** 2019. Aerosol optical properties in the Arctic: The role of aerosol chemistry and dust composition in a closure experiment between Lidar and tethered balloon vertical profiles. *Science of the Total Environment* **686**: 452–467. DOI: http://dx.doi.org/10.1016/j.scitotenv.2019.05.399.

Griesche, HJ, **Ohneiser, K**, **Seifert, P**, **Radenz, M**, **Engelmann, R**, **Ansmann, A.** 2021. Contrasting ice formation in Arctic clouds: Surface-coupled vs. surface-decoupled clouds. *Atmospheric Chemistry and Physics* **21**(13): 10357–10374. DOI: http://dx.doi.org/10.5194/acp-21-10357-2021.

Griesche, HJ, **Seifert, P**, **Ansmann, A**, **Baars, H**, **Velasco, CB**, **Bühl, J**, **Engelmann, R**, **Radenz, M**, **Zhenping, Y**, **Macke, A.** 2020. Application of the shipborne remote sensing supersite OCEANET for profiling of Arctic aerosols and clouds during Polarstern cruise PS106. *Atmospheric Measurement Techniques* **13**(10): 5335–5358. DOI: http://dx.doi.org/10.5194/amt-13-5335-2020.

Hersbach, H, **Bell, B**, **Berrisford, P**, **Hirahara, S**, **Horányi, A**, **Muñoz-Sabater, J**, **Nicolas, J**, **Peubey, C**, **Radu, R**, **Schepers, D**, **Simmons, A**, **Soci, C**, **Abdalla, S**, **Abellan, X**, **Balsamo, G**, **Bechtold, P**, **Biavati, G**, **Bidlot, J**, **Bonavita, M**, **De Chiara, G**, **Dahlgren, P**, **Dee, D**, **Diamantakis, M**, **Dragani, R**, **Flemming, J**, **Forbes, R**, **Fuentes, M**, **Geer, A**, **Haimberger, L**, **Healy, S**, **Hogan, RJ**, **Hólm, E**, **Janisková, M**, **Keeley, S**, **Laloyaux, P**, **Lopez, P**, **Lupu, C**, **Radnoti, G**, **de Rosnay, P**, **Rozum, I**, **Vamborg, F**, **Villaume, S**, **Thépaut, JN.** 2020. The ERA5 global reanalysis. *Quarterly Journal of the Royal Meteorological Society* **146**(730): 1999–2049. DOI: http://dx.doi.org/10.1002/qj.3803.

Heymsfield, AJ, **McFarquhar, GM**. 1996. High albedos of cirrus in the tropical pacific warm pool: Microphysical interpretations from CEPEX and from Kwajalein, Marshall Islands. *Journal of the Atmospheric Sciences* **53**(17): 2424–2451. DOI: http://dx.doi.org/10.1175/1520-0469(1996)053<2424:HAOCIT>2.0.CO;2.

Illingworth, AJ, **Hogan, RJ**, **O'Connor, EJ**, **Bouniol, D**, **Brooks, ME**, **Delanoë, J**, **Donovan, DP**, **Eastment, JD**, **Gaussiat, N**, **Goddard, JW**, **Haeffelin, M**, **Klein Baltinik, H**, **Krasnov, OA**, **Pelon, J**, **Piriou, JM**, **Protat, A**, **Russchenberg, HW**, **Seifert, A**, **Tompkins, AM**, **van Zadelhoff, GJ**, **Vinit, F**, **Willen, U**, **Wilson, DR**, **Wrench, CL.** 2007. Cloudnet: Continuous evaluation of cloud profiles in seven operational models using ground-based observations. *Bulletin of the American Meteorological Society* **88**(6): 883–898. DOI: http://dx.doi.org/10.1175/BAMS-88-6-883.

Knust, R. 2017. Polar research and supply vessel POLARSTERN operated by the Alfred-Wegener-Institute. *Journal of large-scale research facilities JLSRF* **3**: A119–A119. DOI: http://dx.doi.org/10.17815/jlsrf-3-163. Available at http://jlsrf.org/index.php/lsf/article/view/163. Accessed 25 April 2021.

Kylling, A, **Stamnes, K**, **Tsay, SC.** 1995. A reliable and efficient two-stream algorithm for spherical radiative transfer: Documentation of accuracy in realistic layered media. *Journal of Atmospheric Chemistry* **21**(2): 115–150. DOI: http://dx.doi.org/10.1007/BF00696577.

Lampert, A, **Altstädter, B**, **Bärfuss, K**, **Bretschneider, L**, **Sandgaard, J**, **Michaelis, J**, **Lobitz, L**, **Asmussen, M**, **Damm, E**, **Käthner, R**, **Krüger, T**, **Lüpkes, C**, **Nowak, S**, **Peuker, A**, **Rausch, T**, **Reiser, F**, **Scholtz,**

A, **Zakharov, DS**, **Gaus, D**, **Bansmer, S**, **Wehner, B**, **Pätzold, F.** 2020. Unmanned aerial systems for investigating the polar atmospheric boundary layer-technical challenges and examples of applications. *Atmosphere* **11**(4): 416. DOI: http://dx.doi.org/10.3390/ATMOS11040416.

Lonardi, M, **Pilz, C**, **Siebert, H**, **Ehrlich, A**, **Wendisch, M**. 2022a. Tethered balloon-borne measurements of liquid cloud water presence during MOSAiC leg 4 in July 2020 [dataset]. DOI: http://dx.doi.org/10.1594/PANGAEA.944068; https://doi.pangaea.de/10.1594/PANGAEA.944068.

Lonardi, M, **Pilz, C**, **Siebert, H**, **Ehrlich, A**, **Wendisch, M**. 2022b. Tethered balloon-borne measurements of solar radiation during MOSAiC leg 4 in July 2020 [dataset]. DOI: http://dx.doi.org/10.1594/PANGAEA.944232; https://doi.pangaea.de/10.1594/PANGAEA.944232.

Lonardi, M, **Pilz, C**, **Siebert, H**, **Ehrlich, A**, **Wendisch, M.** 2022c. Tethered balloon-borne measurements of terrestrial radiation during MOSAiC leg 4 in July 2020 [dataset]. DOI: http://dx.doi.org/10.1594/PANGAEA.944200; https://doi.pangaea.de/10.1594/PANGAEA.944200.

Maturilli, M, **Holdridge, DJ**, **Dahlke, S**, **Graeser, J**, **Sommerfeld, A**, **Jaiser, R**, **Deckelmann, H**, **Schulz, A**. 2021. Initial radiosonde data from 2019-10 to 2020-09 during project MOSAiC [dataset]. DOI: http://dx.doi.org/10.1594/PANGAEA.928656; https://doi.pangaea.de/10.1594/PANGAEA.928656.

Moon, TA, **Druckenmiller, ML**, **Thoman, RL eds**. 2021. *Arctic Report Card 2021*. DOI: http://dx.doi.org/10.25923/5s0f-5163.

Morrison, H, **de Boer, G**, **Feingold, G**, **Harrington, J**, **Shupe, MD**, **Sulia, K.** 2012. Resilience of persistent Arctic mixed-phase clouds. *Nature Geoscience* **5**: 11–17. DOI: http://dx.doi.org/10.1038/ngeo1332.

Pilz, C, **Düsing, S**, **Wehner, B**, **Müller, T**, **Siebert, H**, **Voigtländer, J**, **Lonardi, M.** 2022. CAMP: A balloon-borne platform for aerosol particle studies in the lower atmosphere. *Atmospheric Measurement Techniques Discussions* **2022**: 1–23. DOI: http://dx.doi.org/10.5194/amt-2022-175. Available at https://amt.copernicus.org/preprints/amt-2022-175/. Accessed 25 June 2022.

Pilz, C, **Lonardi, M**, **Siebert, H**, **Wehner, B.** 2022. Tethered balloon-borne measurements of aerosol particle microphysics during the MOSAiC expedition from June to July 2020 [dataset]. DOI: http://dx.doi.org/10.1594/PANGAEA.943907; https://doi.pangaea.de/10.1594/PANGAEA.943907.

Pithan, F, **Mauritsen, T.** 2014. Arctic amplification dominated by temperature feedbacks in contemporary climate models. *Nature Geoscience* **7**(3): 181–184. DOI: http://dx.doi.org/10.1038/ngeo2071.

Pithan, F, **Svensson, G**, **Caballero, R**, **Chechin, D**, **Cronin, TW**, **Ekman, AM**, **Neggers, R**, **Shupe, MD**, **Solomon, A**, **Tjernström, M**, **Wendisch, M**. 2018. Role of air-mass transformations in exchange between the Arctic and mid-latitudes. *Nature Geoscience* **11**: 805–812. DOI: http://dx.doi.org/10.1038/s41561-018-0234-1.

Rinke, A, **Cassano, JJ**, **Cassano, EN**, **Jaiser, R**, **Handorf, D.** 2021. Meteorological conditions during the MOSAiC expedition. *Elementa: Science of the Anthropocene* **9**(1). DOI: http://dx.doi.org/10.1525/elementa.2021.00023.

Schmale, J, **Arnold, SR**, **Law, KS**, **Thorp, T**, **Anenberg, S**, **Simpson, WR**, **Mao, J**, **Pratt, KA.** 2018. Local Arctic air pollution: A neglected but serious problem. *Earth's Future* **6**(10): 1385–1412. DOI: http://dx.doi.org/10.1029/2018EF000952.

Schmale, J, **Zieger, P**, **Ekman, AM.** 2021. Aerosols in current and future Arctic climate. *Nature Climate Change* **11**(2): 95–105. DOI: http://dx.doi.org/10.1038/s41558-020-00969-5.

Serreze, MC, **Barry, RG.** 2011. Processes and impacts of Arctic amplification: A research synthesis. *Global and Planetary Change* **77**(1–2): 85–96. DOI: http://dx.doi.org/10.1016/j.gloplacha.2011.03.004.

Serreze, MC, **Francis, JA.** 2006. The Arctic amplification debate. *Climatic Change* **76**(3–4): 241–264. DOI: http://dx.doi.org/10.1007/s10584-005-9017-y.

Shupe, MD. 2011. Clouds at Arctic atmospheric observatories. Part II: Thermodynamic phase characteristics. *Journal of Applied Meteorology and Climatology* **50**(3): 626–644. DOI: http://dx.doi.org/10.1175/2010JAMC2468.1.

Shupe, MD, **Persson, PO**, **Brooks, IM**, **Tjernström, M**, **Sedlar, J**, **Mauritsen, T**, **Sjogren, S**, **Leck, C.** 2013. Cloud and boundary layer interactions over the Arctic sea ice in late summer. *Atmospheric Chemistry and Physics* **13**(18): 9379–9399. DOI: http://dx.doi.org/10.5194/acp-13-9379-2013.

Shupe, MD, **Rex, M**, **Blomquist, B**, **Persson, POG**, **Schmale, J**, **Uttal, T**, **Althausen, D**, **Angot, H**, **Archer, S**, **Bariteau, L**, **Beck, I**, **Bilberry, J**, **Bucci, S**, **Buck, C**, **Boyer, M**, **Brasseur, Z**, **Brooks, IM**, **Calmer, R**, **Cassano, J**, **Castro, V**, **Chu, D**, **Costa, D**, **Cox, CJ**, **Creamean, J**, **Crewell, S**, **Dahlke, S**, **Damm, E**, **de Boer, G**, **Deckelmann, H**, **Dethloff, K**, **Dütsch, M**, **Ebell, K**, **Ehrlich, A**, **Ellis, J**, **Engelmann, R**, **Fong, AA**, **Frey, MM**, **Gallagher, MR**, **Ganzeveld, L**, **Gradinger, R**, **Graeser, J**, **Greenamyer, V**, **Griesche, H**, **Griffiths, S**, **Hamilton, J**, **Heinemann, G**, **Helmig, D**, **Herber, A**, **Heuzé, C**, **Hofer, J**, **Houchens, T**, **Howard, D**, **Inoue, J**, **Jacobi, HW**, **Jaiser, R**, **Jokinen, T**, **Jourdan, O**, **Jozef, G**, **King, W**, **Kirchgaessner, A**, **Klingebiel, M**, **Krassovski, M**, **Krumpen, T**, **Lampert, A**, **Landing, W**, **Laurila, T**, **Lawrence, D**, **Lonardi, M**, **Loose, B**, **Lüpkes, C**, **Maahn, M**, **Macke, A**, **Maslowski, W**, **Marsay, C**, **Maturilli, M**, **Mech, M**, **Morris, S**, **Moser, M**, **Nicolaus, M**, **Ortega, P**, **Osborn, J**, **Pätzold, F**, **Perovich, DK**, **Petäjä, T**, **Pilz, C**, **Pirazzini, R**, **Posman, K**, **Powers, H**, **Pratt, KA**, **Preußer, A**, **Quéléver, L**, **Radenz, M**, **Rabe, B**, **Rinke, A**, **Sachs, T**, **Schulz, A**, **Siebert, H**, **Silva, T**, **Solomon, A**, **Sommerfeld, A**, **Spreen, G**, **Stephens, M**, **Stohl, A**, **Svensson, G**, **Uin, J**, **Viegas,**

J, **Voigt, C**, **von der Gathen, P**, **Wehner, B**, **Welker, JM**, **Wendisch, M**, **Werner, M**, **Xie, ZQ**, **Yue, F**. 2022. Overview of the MOSAiC expedition—Atmosphere. *Elementa: Science of the Anthropocene* **10**(1): 00060. DOI: http://dx.doi.org/10.1525/elementa.2021.00060.

Silber, I, **Shupe, MD**. 2022. Insights on sources and formation mechanisms of liquid-bearing clouds over MOSAiC examined from a Lagrangian framework. *Elementa: Science of the Anthropocene* **10**(1): 000071. DOI: http://dx.doi.org/10.1525/elementa.2021.000071.

Sotiropoulou, G, **Sedlar, J**, **Tjernström, M**, **Shupe, MD**, **Brooks, IM**, **Persson, PO.** 2014. The thermodynamic structure of summer Arctic stratocumulus and the dynamic coupling to the surface. *Atmospheric Chemistry and Physics* **14**(22): 12573–12592. DOI: http://dx.doi.org/10.5194/acp-14-12573-2014.

Sprenger, M, **Wernli, H**. 2015. The LAGRANTO Lagrangian analysis tool—Version 2.0. *Geoscientific Model Development* **8**(8): 2569–2586. DOI: http://dx.doi.org/10.5194/gmd-8-2569-2015.

Stroeve, J, **Notz, D**. 2018. Changing state of Arctic sea ice across all seasons. *Environmental Research Letters* **13**(10): 103001. DOI: http://dx.doi.org/10.1088/1748-9326/aade56.

Taylor, PC, **Cai, M**, **Hu, A**, **Meehl, J**, **Washington, W**, **Zhang, GJ**. 2013. A decomposition of feedback contributions to polar warming amplification. *Journal of Climate* **26**(18): 7023–7043. DOI: http://dx.doi.org/10.1175/JCLI-D-12-00696.1.

Tjernström, M, **Shupe, MD**, **Brooks, IM**, **Achtert, P**, **Prytherch, J**, **Sedlar, J**. 2019. Arctic summer airmass transformation, surface inversions, and the surface energy budget. *Journal of Climate* **32**(3): 769–789. DOI: http://dx.doi.org/10.1175/JCLI-D-18-0216.1.

Turner, DD, **Shupe, MD**, **Zwink, AB.** 2018. Characteristic atmospheric radiative heating rate profiles in Arctic clouds as observed at Barrow, Alaska. *Journal of Applied Meteorology and Climatology* **57**(4): 953–968. DOI: http://dx.doi.org/10.1175/JAMC-D-17-0252.1.

Wendisch, M, **Brückner, M**, **Burrows, JP**, **Crewell, S**, **Dethlof, K**, **Ebell, K**, **Lüpkes, C**, **Macke, A**, **Notholt, J**, **Quaas, J**, **Rinke, A**, **Tegen, I.** 2017. Understanding the causes and effects of rapid warming in the Arctic. *Eos (United States)* **98**(8). DOI: http://dx.doi.org/10.1029/2017eo064803.

Wendisch, M, **Macke, A**, **Ehrlich, A**, **Lüpkes, C**, **Mech, M**, **Chechin, D**, **Dethloff, K**, **Velasco, CB**, **Bozem, H**, **BrüCkner, M**, **Clemen, HC**, **Crewell, S**, **Donth, T**, **Dupuy, R**, **Ebell, K**, **Egerer, U**, **Engelmann, R**, **Engler, C**, **Eppers, O**, **Gehrmann, M**, **Gong, X**, **Gottschalk, M**, **Gourbeyre, C**, **Griesche, H**, **Hartmann, J**, **Hartmann, M**, **Heinold, B**, **Herber, A**, **Herrmann, H**, **Heygster, G**, **Hoor, P**, **Jafariserajehlou, S**, **JäKel, E**, **JäRvinen, E**, **Jourdan, O**, **KäStner, U**, **Kecorius, S**, **Knudsen, EM**, **KöLlner, F**, **Kretzschmar, J**, **Lelli, L**, **Leroy, D**, **Maturilli, M**, **Mei, L**, **Mertes, S**, **Mioche, G**, **Neuber, R**, **Nicolaus, M**, **Nomokonova, T**, **Notholt, J**, **Palm, M**, **Van Pinxteren, M**, **Quaas, J**, **Richter, P**, **Ruiz-Donoso, E**, **SchäFer, M**, **Schmieder, K**, **Schnaiter, M**, **Schneider, J**, **SchwarzenböCk, A**, **Seifert, P**, **Shupe, MD**, **Siebert, H**, **Spreen, G**, **Stapf, J**, **Stratmann, F**, **Vogl, T**, **Welti, A**, **Wex, H**, **Wiedensohler, A**, **Zanatta, M**, **Zeppenfeld, S**. 2019. The Arctic cloud puzzle using ACLOUD/PASCAL multiplatform observations to unravel the role of clouds and aerosol particles in arctic amplification. *Bulletin of the American Meteorological Society* **100**(5): 841–871. http://dx.doi.org/10.1175/BAMS-D-18-0072.1.

How to cite this article: Lonardi, M, Pilz, C, Akansu, EF, Dahlke, S, Egerer, U, Ehrlich, A, Griesche, H, Heymsfield, AJ, Kirbus, B, Schmitt, CG, Shupe, MD, Siebert, H, Wehner, B, Wendisch, M. 2022. Tethered balloon-borne profile measurements of atmospheric properties in the cloudy atmospheric boundary layer over the Arctic sea ice during MOSAiC: Overview and first results. *Elementa: Science of the Anthropocene* 10(1). DOI: https://doi.org/10.1525/elementa.2021.000120

Domain Editor-in-Chief: Detlev Helmig, Boulder AIR LLC, Boulder, CO, USA

Guest Editor: MingXi Yang, Plymouth Marine Laboratory, Plymouth, UK

Knowledge Domain: Atmospheric Science

Part of an Elementa Special Feature: The Multidisciplinary Drifting Observatory for the Study of Arctic Climate (MOSAiC)

Published: September 23, 2022 **Accepted:** June 23, 2022 **Submitted:** December 20, 2021